J. Fluid Mech. (1998), *vol.* 361, *pp.* 189–236. Printed in the United Kingdom

Dynamics of counter-rotating vortex pairs in stratified and sheared environments

By J. F. GARTEN, S. ARENDT, D. C. FRITTS AND J. WERNE

Colorado Research Associates, 3380 Mitchell Lane, Boulder, CO 80301, USA

(Received 23 April 1997 and in revised form 1 December 1997)

The evolution of a vertically propagating vortex pair in stratified and sheared environments is studied with a two-dimensional numerical model. We consider a range of Froude (*Fr*) and Richardson (*Ri*) numbers, and a limited number of Reynolds numbers (*Re*). We find that stratification causes the formation of counter-sign vorticity around each of the original vortices through baroclinic production. At higher *Fr*, this wake vorticity advects the primary vortices closer together, decreasing their separation distance and increasing their vertical propagation speed, as predicted by Crow (1974) and Scorer & Davenport (1970). For these higher values of *Fr*, the wake vorticity also participates in an instability of the primary vortex pair, with the direction of propagation of the pair oscillating about the vertical. We term this instability the vortex head instability to distinguish it from the jet instabilities to which the wake itself is also susceptible. At lower *Fr*, internal gravity wave radiation dominates, and the intensity and spatial coherence of each vortex is rapidly reduced.

When a mean horizontal flow having constant shear is present in an unstratified fluid, we find that the vortices eventually rotate about one another with the same rotational sense as the background shear flow, as predicted in Lissaman *et al.* (1973). When stratification is also present, we find that the distribution of baroclinically generated wake vorticity is asymmetric, which sometimes leads to the emergence of a solitary vortex with the same sign as the background shear vorticity (depending on the values of *Fr*, *Ri*, and *Re*). Our limited survey of parameter space indicates that a solitary vortex emerges more rapidly for smaller values of *Ri*, smaller values of *Fr*, and/or larger values of *Re*.

1. Introduction

The evolution of vortex pairs is a problem of longstanding interest. A common example is the trailing vortices which form behind an aircraft due to its lift; these vortices pose a considerable hazard to other aircraft (Olsen, Goldburg & Rogers 1971). Other examples of vortex pairs are found within thermal plumes (Rast 1997) and rising bubbles (Longcope, Fisher & Arendt 1996), as well as within convective instabilities such as those occurring in a breaking gravity wave (e.g. Andreassen *et al.* 1994), and fully developed turbulence (Rogers & Moin 1987).

For a fluid without density stratification or environmental shear, some work (Pierrehumbert 1980) has been done in two dimensions, but much interest has

focused on three-dimensional aspects, principally because the vortices undergo a three-dimensional instability known as the Crow instability (Crow 1970). This long-wavelength instability also has a short-wavelength counterpart (Tsai & Widnall 1976; Moore & Saffman 1975) which is related to zero-frequency Kelvin twist waves (e.g. Saffman 1992), but which generally has a smaller growth rate than the long-wavelength instability.

When density stratification is present, buoyancy complicates the flow, and so most work has been limited to two dimensions. Turner (1960) studied a buoyant vortex pair in a constant-density fluid while Scorer & Davenport (1970), Saffman (1972), Crow (1974), and Hill (1975) studied various aspects of the evolution of a vortex pair in a stratified fluid. Recent experimental work includes Tomassian (1979), Delisi, Robins & Lucas (1991), and Sarpkaya (1983). Recent numerical work includes Jaderberg (1980), Robins & Delisi (1990), Schilling, Siano & Etling (1996), Spalart (1996), and Garten (1997); the last three works show that weak density stratification acts to decrease the vortex pair's separation distance while increasing its propagation velocity, consistent with the predictions of Crow (1974) and Scorer & Davenport (1970). These conclusions appear to be in conflict with experimental results, which do not find acceleration of the vortex pair (except for Tomassian 1979 who finds weak acceleration). This discrepancy is perhaps due to constraints on the value of the Reynolds number in the numerical simulations, and the accompanying restriction to laminar flows. Aspects of the effects of ambient turbulence on the evolution of vortex pairs have been addressed by Crow & Bate (1976), Hecht, Bilanin & Hirsh (1981), and Greene (1986).

At later times in the flow evolution, the vortex pair ceases its usual propagation because of influences of its baroclinically generated wake and attrition by viscous diffusion. Schilling *et al.* (1996) observed a wriggling of the vortex pair, an effect which we also find and which we call the vortex head instability. This instability results in a growing oscillation of the vortex pair propagation direction about the vertical, and in the development of coherent structures near the maximum height attained by the vortex pair. We find that the baroclinically generated wake of the vortex pair is also susceptible to a jet instability which results in greater complexity of the late-time flow. Other authors who study the evolution of vortex pairs in an incompressible fluid have not observed these instabilities, either because of enforced symmetry in their numerical studies, as in the case of Spalart (1996), or because of a lack of seeding with perturbations to excite the instabilities, as in the case of Robins & Delisi (1990). However, the compressible plume studies by Rast (1997) also exhibit the asymmetric evolution we report here.

The report by Lissaman *et al.* (1973) contains a summary of the predicted effects of horizontal shear (with uniform vorticity) on vertically propagating two-dimensional vortex pairs in an unstratified fluid. Owing to the background shear, the re-circulation cells of the two vortices are asymmetric; specifically, the re-circulation cell of the opposite-sign vortex (i.e. the vortex with a sign of vorticity opposite that of the background shear vorticity) is smaller than the re-circulation cell of the same-sign vortex. When the vortices diffuse outwards sufficiently, some of the vorticity from the opposite-sign vortex is detrained (i.e. left behind) by the vortex pair, and the vortex pair consequently rotates with the same rotational sense as the background shear flow. Burnham (1972) and Harvey & Perry (1971) also considered this problem, but with a non-uniform shear. Robins & Delisi (1990) presented numerical simulations of two-dimensional vortex pairs in an environment that was both stratified and uniformly sheared. The results summarized in their figure 13 indicate that for certain Froude

(Fr) and Richardson (Ri) numbers, a solitary vortex emerges† possessing the same sign as the background shear vorticity.

The present paper presents two-dimensional simulations of vortex pairs in stratified and sheared environments. Our purpose is to examine the underlying physical processes controlling the dynamics of such vortex pairs, in particular the interaction of the vortex pair with the vorticity in its baroclinically generated wake. Of particular interest are the theories formulated by Saffman (1972) and Crow (1974) that predict the time evolution of the separation distance and the vertical position of the vortex pair. One of the assumptions of Saffman's model is that the separation distance between the vortices remains constant as the flow evolves; we find that this is only true during an early adjustment phase. Once the flow is mature, the evolution of vortex pairs at higher Froude numbers (stronger inertial forces relative to buoyancy forces) is in qualitative agreement with Crow's theory. Even in the lower Froude number regime, we find that the separation distance does not remain constant, but rather increases with time. Finally, neither theory predicts the late-time viscous behaviour, something which is of concern for numerical simulations as these are necessarily constrained to lower values of the Reynolds number.

The paper is organized as follows. In § 2, we discuss the numerical model and its limitations. In § 3, we address the effects of stratification on a vertically propagating, counter-rotating vortex pair by examining a range from weak to strong stratification, and we compare our results to the predictions of the Crow and Saffman theories. In § 4, we investigate the consequences of seeding the initial flow field with perturbations, and we discuss two distinct instabilities. In § 5, we consider the effects of an environmental shear on the evolution of vortex pairs, and discuss the effect of stratification on the emergence of a single vortex. Finally, we summarize our main conclusions in § 6.

2. Numerical model

2.1. *Basic equations and numerical method*

We use a numerical model based on the Boussinesq approximation to the two-dimensional Navier-Stokes equations. The full density ($\tilde{\rho} = \bar{\rho} + \rho$) and temperature ($\tilde{T} = \bar{T} + T$) are expanded in terms of horizontal mean (overbar) and perturbation quantities.‡ The equation of state that relates the two fields is

$$\frac{\rho}{\rho_0} = -\alpha T, \tag{2.1}$$

where α is the thermal expansion coefficient and ρ_0 is a reference value.

The background temperature is $T = \beta z$ so that the buoyancy frequency N is given by $N^2 = g\alpha\beta$, where g is the acceleration due to gravity. The equations of motion (the non-dimensionalization will be discussed in the next section) are then

$$\nabla \cdot \boldsymbol{v} = 0, \tag{2.2}$$

$$\frac{\partial \boldsymbol{v}}{\partial t} + \boldsymbol{\omega} \times \boldsymbol{v} = -\nabla\pi + \frac{T}{Fr^2}\hat{z} + \frac{1}{Re}\nabla^2\boldsymbol{v}, \tag{2.3}$$

$$\frac{\partial T}{\partial t} + (\boldsymbol{v} \cdot \nabla)(\bar{T} + T) = \frac{1}{Re\ Pr}\nabla^2 T, \tag{2.4}$$

† Robins & Delisi define a solitary vortex emerging as one vortex being 40% stronger than the other.

‡ The model also permits unstratified simulations for comparison to the stratified and sheared cases.

where $\boldsymbol{v} = (0, v, w)$ is the velocity, $\boldsymbol{\omega} = \nabla \times \boldsymbol{v} = (\omega_x, 0, 0)$ is the vorticity, π is the dynamic pressure head, and Re and Pr are the Reynolds and Prandtl numbers to be defined in § 2.2.†

We use a pseudo-spectral, stream-function/vorticity, Galerkin method (Canuto *et al.* 1988) to solve (2.2)–(2.4), representing the field variables with Fourier polynomials of the form

$$A(y,z,t) = \sum_{m=-N_y/2}^{N_y/2} \sum_{n=-N_z/2}^{N_z/2} \hat{A}_{mn}(t) \exp\left[2\pi \mathrm{i}\left(\frac{my}{L_y}\right)\right] \exp\left[2\pi \mathrm{i}\left(\frac{nz}{L_z}\right)\right], \tag{2.5}$$

where N_y and N_z are the number of collocation points in the y- and z-directions, and L_y and L_z are the domain lengths. Dealiasing with the 2/3 rule is used in all spatial directions (Canuto *et al.* 1988).

Differentiations are accomplished with multiplications by k-vectors in Fourier space so that the velocity components v and w are related to ω_x through

$$\hat{v}_{mn} = \mathrm{i}\frac{k_z}{k^2}\hat{\omega}_{mn}, \quad \hat{w}_{mn} = -\mathrm{i}\frac{k_y}{k^2}\hat{\omega}_{mn}, \tag{2.6}$$

where $k_y = 2\pi m/L_y$, $k_z = 2\pi n/L_z$, and $k^2 = k_y^2 + k_z^2$. Taking the curl of (2.3), the evolution equation for ω_x is

$$\frac{\partial \omega_x}{\partial t} = -\nabla \cdot (\boldsymbol{v}\omega_x) + \frac{1}{Fr^2}\frac{\partial T}{\partial y} + \frac{1}{Re}\nabla^2 \omega_x. \tag{2.7}$$

Solutions are obtained by time-advancing (2.4) and (2.7).

We use a hybrid implicit/explicit third-order Runga–Kutta scheme developed by Spalart, Moser & Rogers (1991) to time-advance the variables. Diffusive and buoyancy terms are handled implicitly in spectral space, while nonlinear terms are treated explicitly in physical space, then projected to Fourier space using fast Fourier transforms (FFTs). The timestep δt is variable, selected in accord with the maximum velocity/grid-spacing ratio $U = \max|u/\delta r|$ (u is one component of the flow velocity and δr the grid spacing parallel to that velocity) and the Courant–Friedrichs–Lewy (CFL) condition, $\delta t = \mathrm{CFL}/U$. We typically use values of CFL between 0.65 and 0.70 (for the full, three-level Runge–Kutta timestep).

In many of our solutions, resolution requirements are time-dependent, increasing (or decreasing) by a factor of four or more during the flow evolution. Interpolation (or deterpolation) of field variables allows for frugality with finite numerical resources, and is accomplished by expressing the field variables in Fourier space and adding zeros for the coefficients of the new, higher-wavenumber modes (or simply zeroing coefficients above the new highest wavenumber).

The boundary conditions in either direction may be chosen to be either periodic or stress-free with zero normal velocity. In all of our unsheared cases, the boundary conditions are periodic in both directions, while in the sheared cases, the horizontal boundary condition is periodic and the vertical is stress-free. This is necessary to accommodate the vertical distribution of horizontal shear velocity, which is of uniform slope for the middle 75% of the domain, and tails off to constant values near the vertical boundaries. For these sheared calculations, the vortex pairs remain within the inner region throughout their evolution (they are never within $3b_0$ of the outer

† Note that together (2.1) and (2.4) imply direct diffusion of density, a disquieting notion which is nevertheless an inherent feature of the Boussinesq approximation.

regions), and the entire shear velocity distribution remains constant within less than 0.01% during the simulation.

With periodic horizontal boundaries, the simulations differ from the ideal case of infinite horizontal extent. In particular, image vortices are present in the simulations, and these contribute to the vertical velocity of the primary vortex pair, reducing it below the value for an infinite domain. For the domain widths we use here, $6b_0$, $8b_0$, and $12b_0$, the initial rise velocity of the vortex pair, in normalized units, is then 0.909, 0.949, and 0.977, respectively, and not 1.0, as would be the case for infinite horizontal extent. The differences, though small, will be important when comparing to theoretical predictions.

2.2. *Initial conditions and non-dimensionalizations*

To model a counter-rotating vortex pair, we use Gaussian distributions of vorticity, with motion confined to the (y, z)-plane. The only non-zero component of the vorticity, $\boldsymbol{\omega}$, is ω_x, and its initial distribution is given by

$$\omega_x(y, z, t = 0) = \omega_0 \exp\left(\frac{-((y - y_1)^2 + (z - z_1)^2)}{2\sigma^2}\right) - \omega_0 \exp\left(\frac{-((y - y_2)^2 + (z - z_2)^2)}{2\sigma^2}\right), \tag{2.8}$$

where ω_0 is the peak magnitude of vorticity for each vortex, σ is a vortex core size, and (y_1, z_1) and (y_2, z_2) are the initial coordinates of the two vortices. For our purposes here, $y_1 < y_2$ ($y_2 - y_1 = b_0$, the initial vortex core separation distance), $z_1 = z_2$, and $\omega_0 > 0$ so that the vortex pair propagates upwards.

Taking the flow to satisfy $\nabla \cdot \boldsymbol{v} = 0$, we find the initial velocity distribution from (2.2) and $\boldsymbol{\omega} = \nabla \times \boldsymbol{v}$:

$$\left.\begin{aligned} v(y, z, t = 0) &= -\frac{\sigma^2 \omega_0 (z - z_1)}{(y - y_1)^2 + (z - z_1)^2}\left(1 - \mathrm{e}^{-((y-y_1)^2+(z-z_1)^2)/2\sigma^2}\right) \\ &\quad + \frac{\sigma^2 \omega_0 (z - z_2)}{(y - y_2)^2 + (z - z_2)^2}\left(1 - \mathrm{e}^{-((y-y_2)^2+(z-z_2)^2)/2\sigma^2}\right), \\ w(y, z, t = 0) &= \frac{\sigma^2 \omega_0 (y - y_1)}{(y - y_1)^2 + (z - z_1)^2}\left(1 - \mathrm{e}^{-((y-y_1)^2+(z-z_1)^2)/2\sigma^2}\right) \\ &\quad - \frac{\sigma^2 \omega_0 (y - y_2)}{(y - y_2)^2 + (z - z_2)^2}\left(1 - \mathrm{e}^{-((y-y_2)^2+(z-z_2)^2)/2\sigma^2}\right). \end{aligned}\right\} \tag{2.9}$$

All of our simulations are performed with a non-dimensional set of equations. Length, velocity, and temperature are reported in units of b_0, W_0 and β, where W_0 is the magnitude of the initial vertical induced velocity and β is the background temperature gradient. Other quantities are measured in units resulting from combinations of these three variables; e.g. time is reported in units of b_0/W_0. Important combinations of these and other parameters form non-dimensional quantities which we will use to characterize our solutions. These include Fr, Re, Pr (Prandtl number), and Ri, which are described below.

The Froude number is defined as

$$Fr = \frac{W_0}{Nb_0}, \tag{2.10}$$

where N is the buoyancy frequency of the background stratification. Hence, Fr is the ratio of the buoyancy time scale to the vortex-pair advection time scale. In the nonlinear regime ($Fr > 1$) the advective effect of each vortex on the other is greater than buoyancy effects, while in the linear regime ($Fr < 1$) the opposite is true. The labels linear and nonlinear refer to the nature of the underlying flow equations in these regimes. From (2.9) and (2.10), we have

$$|\omega_0| = FrN\frac{b_0^2}{\sigma^2}\left(1 - \mathrm{e}^{-b_0^2/2\sigma^2}\right)^{-1}. \tag{2.11}$$

Hence, the initial velocity distribution is specified in terms of Fr, N, b_0, and σ.

The Reynolds number,

$$Re = \frac{W_0 b_0}{\nu}, \tag{2.12}$$

is the ratio of the advective time scale (b_0/W_0) to the viscous time scale (b_0^2/ν), where ν is the coefficient of kinematic viscosity. In the literature, the Reynolds number is often defined in terms of the circulation, $\Gamma = 2\pi W_0 b_0$, so that $Re' = \Gamma/\nu = 2\pi Re$. Therefore, to compare our solutions with these, our Re should be multiplied by 2π. The number of grid points used limits the value of Re that can be attained numerically. In order to investigate the implications of the constraint on Re, we have performed unstratified simulations at $Re = 1000$ and at $Re = 1500$. We find, for example, that the time taken to travel 15 vortex-pair separation distances decreases by only about 1% at the higher Re. From this, it is tempting to conclude that increasing Re beyond 1500 will not significantly affect the results. However, this is not necessarily true, as we will discuss throughout the paper.

The Richardson number, Ri, characterizes the background shear flow. It is equivalent to the square of the ratio of the shear time scale $(\partial V/\partial z)^{-1}$ to the buoyancy time scale N^{-1}:

$$Ri = \frac{N^2}{(\partial V/\partial z)^2}, \tag{2.13}$$

where V is the horizontal flow due to the the mean shear. $Ri = \infty$ corresponds to the case in which there is no mean shear flow present.

The Prandtl number, $Pr = \nu/\kappa$, is the ratio of the diffusive time scale (b_0^2/κ) to the viscous time scale (b_0^2/ν). The value of Pr determines how quickly thermal gradients diffuse relative to velocity gradients. For all of the simulations reported here, $Pr = 1$.

For most of our simulations, the vortex core size is chosen to be $\sigma = b_0/8$; for this choice, the vortices are small enough to be distinct entities but large enough to be adequately resolved in the computation. The vortices are initially placed symmetrically about the centre of the domain. To prevent significant interaction with image vortices (which arise due to the boundary conditions), the horizontal width of the computational domain L_y is made large compared to b_0; specifically we choose $L_y = 6b_0$ for the high-Fr unsheared cases and even greater widths for the low-Fr and sheared cases. The depth of the computational domain depends on the specific needs of each numerical simulation; neither the vortex pair nor its wake are allowed to come within $2b_0$ of the top or bottom of the computational domain.

In § 4, we discuss instabilities of the evolving flow field. Perturbations are required

to excite these instabilities. Seeding with random or 'white' noise is not very effective, as such noise is largely viscously damped out before having any substantial effect on the flow. Instead, a weak but coherent perturbation flow given by

$$v_p = 0.01 \sum_{n=1}^{2N_z/3} n^{-5/3} \sin(2\pi nz/L_z), \tag{2.14}$$

$$w_p = 0.01 \sum_{m=1}^{2N_y/3} m^{-5/3} \sin(2\pi my/L_y) \tag{2.15}$$

is added to the initial conditions. Note that the noise variance decreases with wavenumber and that the perturbation has components that are antisymmetric about the centreline between the two vortices.

2.3. *Numerical resolution*

For simulations of turbulent flows, a typical measure of numerical resolution quality (Henshaw, Kreiss & Reyna 1989) is the ratio of the grid spacing to the Kolmogorov (or dissipation) scale, ℓ_K (Kolmogorov 1941). When temperature stratification is present, resolution of features in the temperature must also be considered. For large Pr, ℓ_K is no longer the smallest scale of the flow, and should be replaced in the resolution criterion by the Batchelor scale, $\ell_B = Pr^{1/2}\ell_K$ (Batchelor 1959; Werne 1993). Though these criteria prove useful when resolution requirements are constrained by turbulence, they do not apply to flows dominated by thin laminar structures. Unfortunately, this is the case for the simulations we present here.

The thin laminar features are caused by the presence of the density stratification and the advection of the density by the flow field. In the constant-density case ($Fr \to \infty$), the resolution needs for our vortex pair are maximum at the initial time, and the initial resolution (assuming the initial fields are resolved) is adequate throughout the entire simulation, and can even be decreased as viscous processes diffuse the vortex cores. In the other limit ($Fr \to 0$), the resolution needs are again maximum at the initial time, since the flow becomes linear and is dominated by internal waves. However, for intermediate values of Fr, the resolution requirements are not maximum at the initial time. As a vortex pair rises, a plume forms, consisting of the fluid advected by the vortex pair. For intermediate values of Fr ($Fr \sim 1$), this plume becomes internally well-mixed more rapidly than its boundaries diffuse (see e.g. figure 2). Sharp horizontal gradients in the temperature field form with scales smaller than the initial flow scales, so that the resolution needs increase. Even after these horizontal gradients begin to diffuse, the resolution needs do not necessarily decrease or even level off. As the vortex pair propagates to even greater heights, sharp vertical thermal gradients develop which again have an impact on the resolution requirements.

Spalart (1996) has proposed quantifying the resolution needs in terms of the length scale of the internal density layers formed by the initial strain at the stagnation points of the vortex pair. In so doing, Spalart implicitly hits upon the critical aspect limiting the resolvability of these simulations, i.e. sharp but laminar density gradients. We feel Spalart's resolution estimates must be refined before they are useable. For example, the criterion does not account for the time-varying (increasing) resolution needs we observe in our solutions, and also lacks the Fr-dependence that we would expect. However, it is possible that the strain rate could be used to judge the resolution requirements if it were computed as the flow evolves. Although the Fr and Re dependencies which are missing from the criteria might then be found in the time-

dependent strain rate, even this method would miss the increasing need for horizontal resolution that we observe in our solutions.

Lacking a reliable method for determining the quality of resolution of our solutions, we have fallen back on the method of looking for Gibbs' oscillations and/or numerical ringing throughout the flow evolutions. For example, very slight ringing is evident in figure 17 (*d*) (near $(y, z) = (2.5, 1.5)$) in the temperature for a simulation with $Fr = 2$, $Ri = 1$, and $Re = 1000$. The run shown in Fig. 17 (*d*) is the least resolved of all the calculations we present here, and all of the other calculations show little sign of numerical ringing (see e.g. figure 2).

3. Stratification effects

In this section, we examine the effects of stable stratification on counter-rotating Gaussian vortex pairs. The stable stratification results in the formation of counter-sign vorticity which plays a crucial role in the resulting dynamics and subsequent evolution of the flow.

3.1. *Review of theory*

The results of our numerical simulations will be compared to two theories which appear to be contradictory and even mutually exclusive. We provide a brief description of each of these theories, paying particular attention to the assumptions and resulting limitations of each.

3.1.1. *Saffman's theory*

Saffman's (1972) model for the motion of a two-dimensional vortex pair in a stratified fluid applies the concept of impulse to an inhomogeneous fluid where the density differences are small. The key assumptions of this inviscid model are that the distance between the vortices and the area of fluid carried with the vortices remain constant, and that the variations of external density near the vortex pair are negligible.

According to this model, the vertical velocity of the vortex pair, $W = \mathrm{d}Z/\mathrm{d}t$, satisfies the equation

$$\frac{\mathrm{d}}{\mathrm{d}t}[(c\bar{\rho}(Z) + \bar{\rho}(0))W] = [\bar{\rho}(Z) - \bar{\rho}(0)]g, \tag{3.1}$$

where $\bar{\rho}(Z)$ is the background density stratification, $\bar{\rho}(0)$ is the density at the starting level, and c is a shape factor which Saffman estimates to be 1.2 for small core sizes. This equation reflects the basic physics: the vortex pair starts with an initial momentum which is decreased by the gravitational force. The details (e.g. where exactly in the flow the momentum is lost) are ignored.

In the case of uniform stratification, $\bar{\rho}(Z) = \bar{\rho}(0)(1 - ZN^2/g)$, the model has a particularly interesting result. The small values of N which are of typical interest allow the replacement of $\bar{\rho}(Z)$ by $\bar{\rho}(0)$ on the left-hand side of (3.1), and the equation of motion for the vortex pair is then

$$\frac{\mathrm{d}^2Z}{\mathrm{d}t^2} + \frac{N^2}{1+c}Z = 0. \tag{3.2}$$

With $Z(0) = 0$ and $W(0) = W_0$ the solution is then

$$Z = \frac{W_0}{\Omega}\sin(\Omega t), \quad \Omega = \frac{N}{(1+c)^{1/2}}. \tag{3.3}$$

Thus, Saffman's model predicts that a vortex pair in uniform stratification will oscillate about its initial vertical position with an amplitude of $|W_0/\Omega|$ and period $2\pi/\Omega$. To put this result in perspective, recall that a pair of counter-rotating vortices without density stratification will self-advect in a straight line at a constant speed, apart from viscous dissipation and advective core deformation.

Although Saffman admits that under normal circumstances three-dimensional processes (i.e. the Crow instability) occur too rapidly for this oscillation to be observed, he leaves open the possibility that it could be observed when stability is locally strong. We are unaware of any numerical results that confirm the undamped oscillation predicted by this model, but the numerical results we present below show that Saffman's model applies within an early adjustment phase of the vortex pair's evolution.

3.1.2. *Crow's theory*

Crow's (1974) model relies on a deeper understanding of the intricate consequences of buoyancy. Buoyancy results in the formation of secondary, baroclinically generated regions of vorticity, which then interact with the primary (original) vortex pair. The key assumptions of Crow's model are that the circulation of each primary vortex remains largely fixed, the stratification is weak, the secondary (baroclinically generated) vorticity is overwhelmingly detrained from the primary vortices, and the flow is considered to be mature and quasi-steady. By mature, we mean that wake vorticity, which is initially zero, has had time to build up. In what follows, we review Crow's model (following Spalart 1996).

As a counter-rotating vortex pair rises in a stratified fluid ($\bar{\rho}(Z) = \bar{\rho}(0)(1-ZN^2/g)$, as above), density gradients increase at the boundary between the fluid elevated (depressed) by the vortex pair and the surrounding fluid. These density gradients result in the formation of opposite-sign vorticity; negative vorticity is formed to the left of the positive primary vortex and positive vorticity is formed to the right of the negative primary vortex. The greater the vertical displacement of the vortex pair from its starting point, the larger the amount of secondary vorticity that is formed. The buoyant creation of secondary vortex circulation ($\pm\Gamma_2$) is of order N^2bZ, where b is the time-dependent vortex separation distance.

While this secondary vorticity is continually created, it is also largely detrained by the motion of the primary vortex pair. The detrained vorticity results in the formation of long thin vortex sheets which stretch from the vortex pair to beyond their initial position. The change in the secondary vortex circulation due to the detrainment is of order $\Gamma_1\Gamma_2/b^2$ where Γ_1 is the primary vortex circulation. The buoyant creation and the subsequent detrainment dominate the evolution of the secondary vorticity. Assuming a steady flow, we equate the two to find

$$\Gamma_2 = C_1\frac{b^3N^2Z}{\Gamma_1}, \tag{3.4}$$

where we have adopted the notation for C_1 (and C_2 and C to follow shortly) used by Spalart (1996).

Now, consider the motion of the primary vortices. To leading order, the vortex-pair rise velocity is given by

$$\frac{\mathrm{d}Z}{\mathrm{d}t} = \frac{\Gamma_1}{2\pi b}. \tag{3.5}$$

The secondary regions of vorticity are more concentrated below the primary vortices than above, and so they advect the primary vortices inwards. To leading order, the

separation distance of the primary vortices varies as

$$\frac{\mathrm{d}b}{\mathrm{d}t} = C_2 \frac{\Gamma_2}{b}. \tag{3.6}$$

Assuming that Γ_1 is constant, (3.4)–(3.6) may be solved to find

$$Z = \frac{\Gamma_1}{(2\pi C)^{1/2} N b_0} \sinh\left(\left(\frac{C}{2\pi}\right)^{1/2} Nt\right), \quad b = \frac{b_0}{\cosh\left(\left(\frac{C}{2\pi}\right)^{1/2} Nt\right)},$$

$$\Gamma_2 = \frac{b^3 N \Gamma_1 C_1}{(2\pi C)^{1/2} b_0 \Gamma_1} \sinh\left(\left(\frac{C}{2\pi}\right) Nt\right), \tag{3.7}$$

where $C = C_1 C_2$. The constant C has been calculated separately by Scorer & Davenport (1970), Spalart (1996), and apparently Crow (referred to by Spalart). For the purposes of comparison with our numerical results we will use the value $C = 2.85$ (Saffman 1972).

In summary, Crow's model predicts that a vortex pair in stratification will drift together and accelerate exponentially as its separation distance decreases. The secondary baroclinically generated vorticity is largely detrained from the primary vortex pair, and causes the inward drift of the primary vortices. Crow's model is inviscid; in a viscous fluid, the continual decrease of the separation distance will eventually lead the primary vortices to diffuse into each another, after which the model no longer applies. Crow's model has previously shown good agreement with numerical simulation results (Spalart 1996); in the next section, we show that our results agree qualitatively with Crow's model after an initial adjustment phase.

3.2. *Flows dominated by advection*

We begin our discussion of specific examples with the nonlinear regime, wherein advective processes are somewhat more important than buoyant processes. We will compare the results of the simulations to the predictions of the theories, and examine the consequences of varying Fr and/or Re.

3.2.1. *Upwards-propagating vortex pair at $Fr = 2$*

We first consider an upwards-propagating vortex pair with $Fr = 2$ and $Re = 1000$ (note that the comparable Reynolds number defined with the circulation is 6283). The computational domain size for this simulation is $6b_0 \times 18b_0$, while the resolution needs maximize at 512×1536 Fourier modes.

Contours of vorticity detailing the early evolution of the vortex pair are displayed in figure 1. This plot, as well as many subsequent plots, contain only the most relevant part of the computational domain. The primary vortices advect one another upwards, while secondary regions of baroclinically generated vorticity (see below) form and grow. The secondary vorticity is largely left behind by the primary vortices, and concentrates in the region to the side of and just behind the primary vortices (see e.g. $t = 3$). As discussed in the summary of Crow's theory, these secondary regions of vorticity advect the primary vortices together (see e.g. $t = 4$); the primary vortices then accelerate upwards.

Contours of the density are shown in the left-hand panels of figure 2. Apart from the diffusive effects in (2.4), the density is a conserved scalar of the flow, and its contours provide a sense of the flow's history. In particular, they show that relatively heavier fluid is entrained by the vortex pair and carried upwards. By $t = 4$, this region

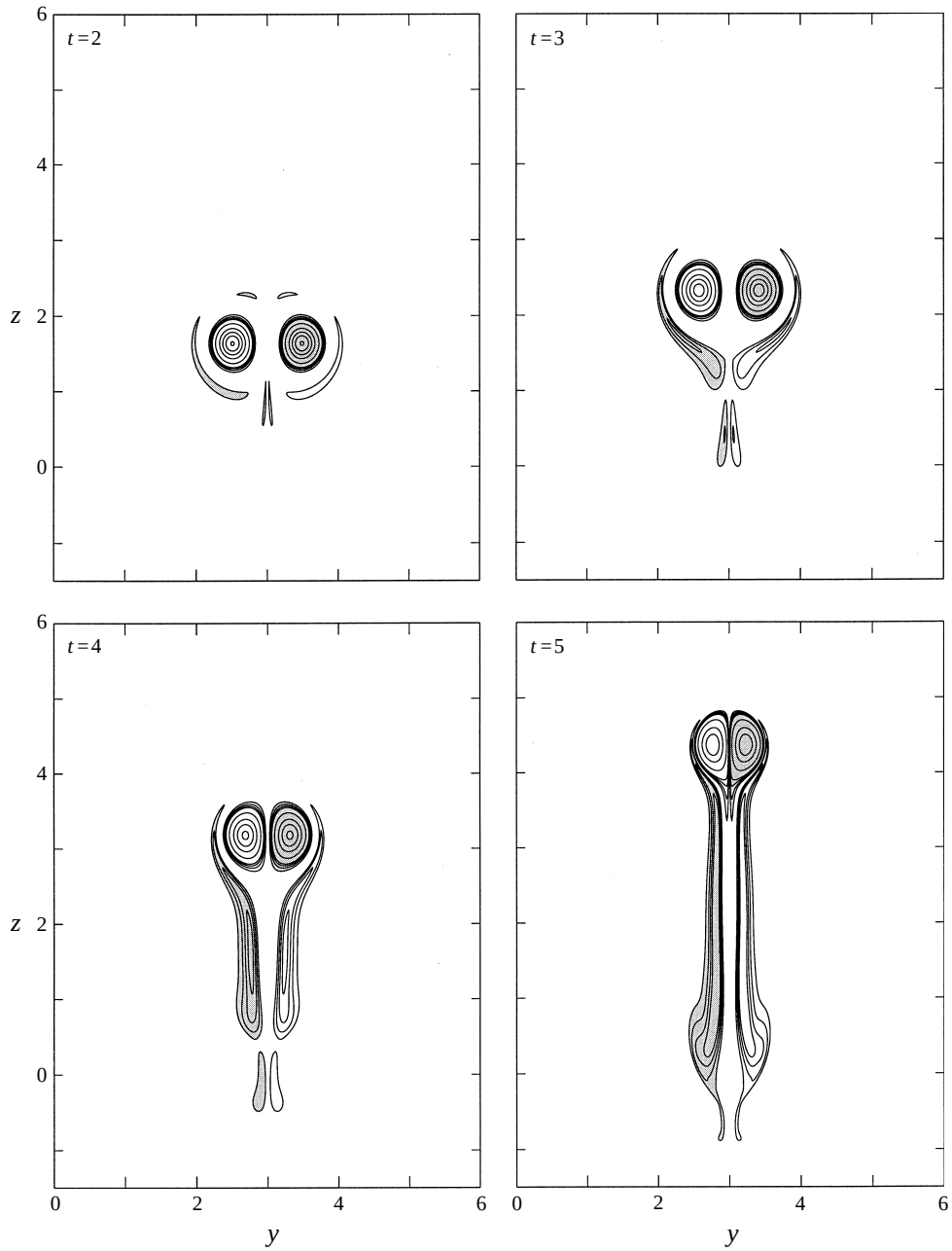

FIGURE 1. Contours of vorticity for an upwards-propagating vortex pair having $Fr = 2$ and $Re = 1000$. Contour levels at $\pm 10, \pm 20, \pm 30$, etc. show the distribution of high-magnitude vorticity, principally the original vortex pair. Contour levels at $\pm 2, \pm 3, \pm 4$ and ± 5 illustrate the distribution of low-magnitude vorticity, principally the baroclinically generated wake. All regions enclosed by negative contours are shaded.

of fluid is internally well mixed, but its boundaries have sharp gradients (note the large density gradients both at the stagnation point at the leading edge of the pair and to either side of the pair). As discussed in § 2.3, numerical noise appears here if the resolution is not increased sufficiently. At later times (not shown here), fluid

initially displaced upwards collapses back downwards due to buoyancy, particularly at the level of excitation of the vortex pair, and overshoots its original position.

To understand the evolution of the flow more fully, it is useful to consider the vorticity equation, which is

$$\frac{\partial \omega_x}{\partial t} = -\nabla \cdot (\boldsymbol{v}\omega_x) + \frac{1}{Fr^2}\frac{\partial T}{\partial y} + \frac{1}{Re}\nabla^2 \omega_x. \tag{3.8}$$

The first term on the right-hand side of this equation is the advection term (through which vorticity is advected as a scalar by the flow), the second is the baroclinic production term (through which vorticity is created by density gradients), and the third is the viscous diffusion term.

Consider the baroclinic production term, which is the cross-product of the horizontal density gradient (due to the upwards/downwards advection of relatively heavier/lighter fluid) with the background pressure gradient (contained within N in Fr). This term represents the vorticity created by the torque of the buoyancy force acting on fluid having a horizontal density gradient. From the perspective of vorticity dynamics, this term contains all buoyancy effects, and so the subsequent effects due to baroclinically generated vorticity may alternatively be viewed as being due to buoyancy.

To see that the secondary regions of vorticity in figure 1 arise from baroclinic production, contours of the baroclinic source are shown in the right-hand panels of figure 2. Since density maxima occur at the centres of the vortices, negative/positive vorticity forms to the left/right of each vortex. Additional counter-sign vorticity forms behind the vortices due to the density perturbations at those locations.

By $t \simeq 3$, the baroclinically generated sheets of vorticity begin to have significant advective effects on the primary vortices (see figure 1). As described in the summary of Crow's theory, the clockwise flow induced by the secondary region of negative vorticity to the left of and below the positive primary vortex advects the positive primary vortex towards the negative primary vortex. In the same manner, the negative primary vortex is advected towards the positive primary vortex. The primary vortices accelerate dramatically as their separation decreases.

Contours of vorticity at more advanced times are shown in figure 3. The vortex pair continues to advect upwards, and the baroclinic production of vorticity results in two long slender vortex sheets extending from the vortex pair to its initial position. Physically, the vertical jet of fluid described by these vortex sheets is due to the buoyancy of the fluid displaced by the vortex pair's advection and entrainment; upwards-displaced fluid rebounds back downwards due to buoyancy. This jet of fluid is also susceptible to an instability which we will discuss in § 4.2.

Finally, near the initial position of the vortex pair, heavier fluid that has escaped the influence of the vortices descends and overshoots this position. A new baroclinically generated semi-coherent vortex pair forms at $t \simeq 6$ near the initial position of the primary vortex pair, and creates its own baroclinically generated wake (e.g. $t = 12$ of figure 3). By $t \simeq 12$, this fluid is again moving upwards due to buoyancy, and what is left of these secondary vortices interacts and dissipates. This process continues, growing weaker in time, until all of the energy is propagated away as internal waves or viscously dissipated.

3.2.2. *Consequences of changing Fr, Re, or σ/b_0.*

We now consider the consequences of varying some of the parameters, beginning with the implications of increasing Re. The advantage in increasing Re is that the flow then approximates real-world flows more closely, while the disadvantage is that the

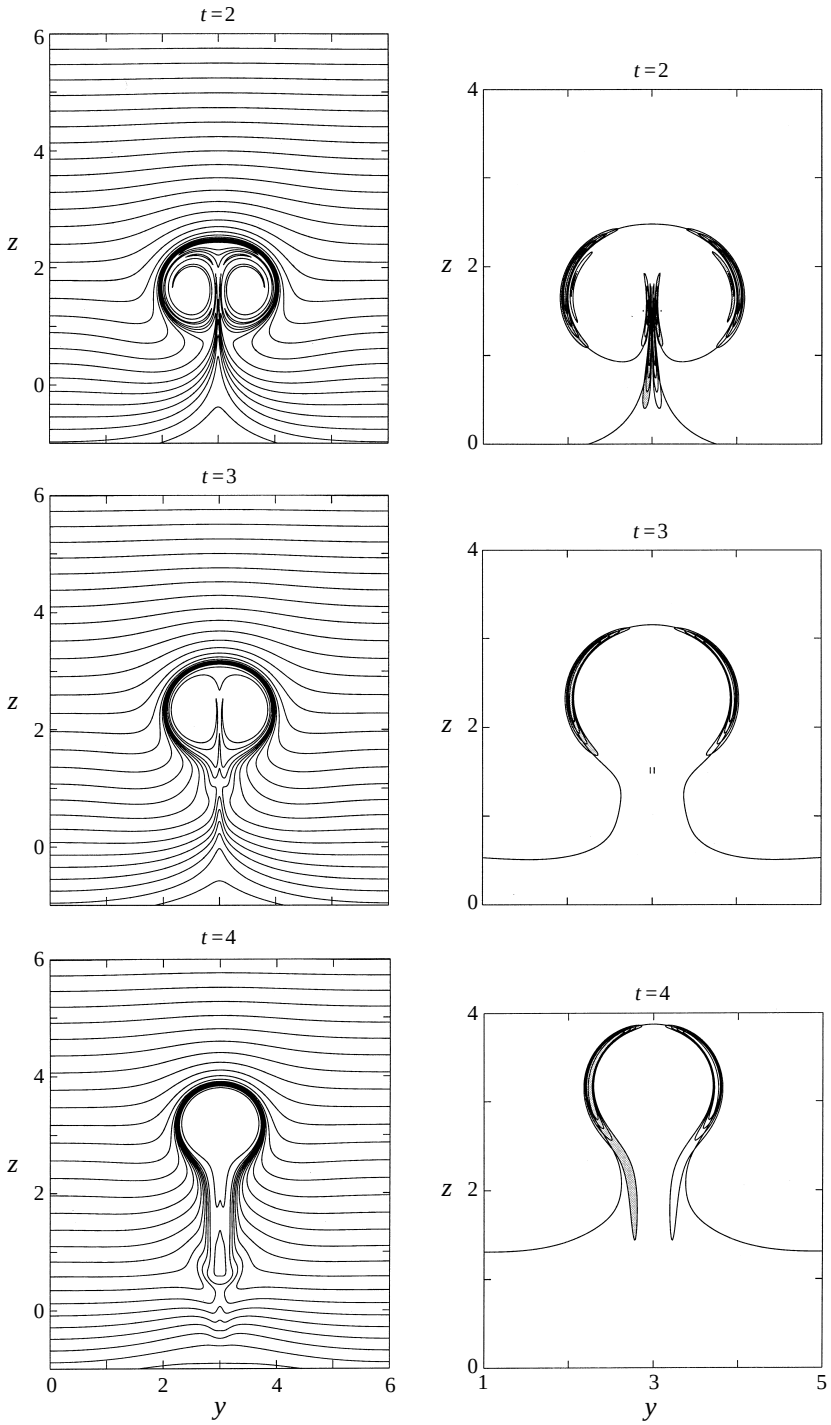

FIGURE 2. Contours of the density (left-hand column) and the baroclinic source of vorticity (right-hand column) for an upwards-propagating vortex pair having $Fr = 2$ and $Re = 1000$. Density contours are at intervals of 0.259, while the contours of the baroclinic source are shown at $\pm 2, \pm 3, \pm 4$ and ± 5. Regions enclosed by negative contours are shaded.

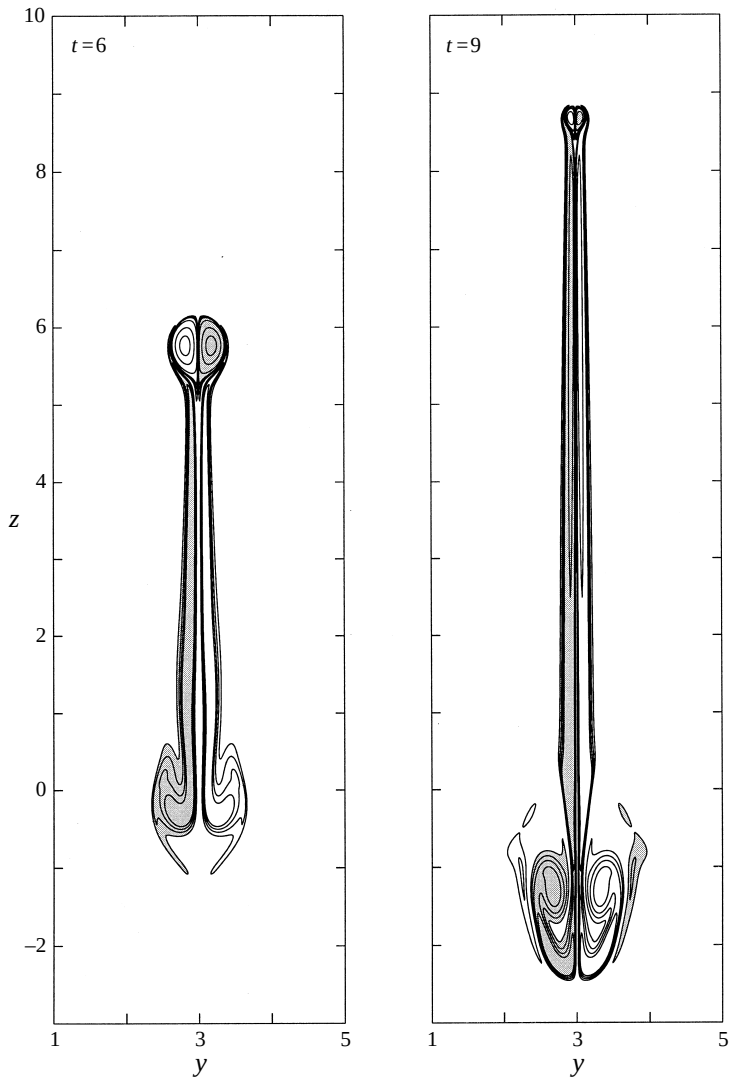

FIGURE 3. For caption see facing page.

required numerical resolution increases. For intermediate values of Fr, the resolution needs in each spatial direction increase by more than a factor of $Re^{1/2}$, a factor used in numerical simulations of turbulent flows.

Contours of vorticity summarizing the evolution of a vortex pair with $Fr = 2$ and $Re = 1500$ are displayed in figure 4. The resolution needs for this simulation maximize at 1024×3072 spectral modes; in this situation, roughly twice as many modes are required in each spatial direction to raise Re by only 50%. On the whole, the results of this numerical simulation are very similar to those of the first. The density gradients are somewhat sharper, and so the baroclinically generated vorticity is concentrated into thinner sheets ($t = 3, 4$). The more strongly concentrated vorticity sheets still form a semi-coherent vortex pair at their head, and this pair propagates slightly farther ($t = 6$) at this higher Re. Upon close inspection, the primary vortices retain more of their original circulation for longer times, and so also propagate farther.

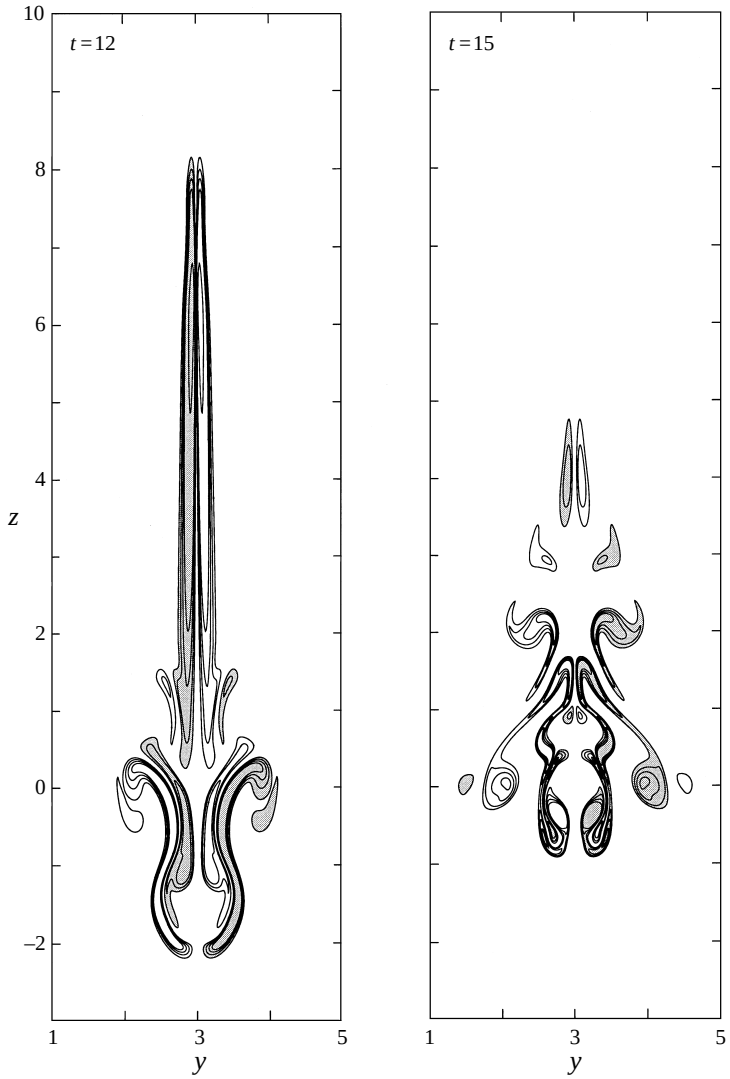

FIGURE 3. As in figure 1, but for more advanced times in the flow.

The vertical positions and separation distances of the vortex pairs at the two different values of Re are compared with the predictions of the Saffman and Crow theories in figure 5. The character of the motion for the two values of Re is very similar. The early behaviour follows the prediction of Saffman's theory at both values of Re; note that the separation distance remains fixed during this early time. After this initial adjustment phase, the character of the curves follows Crow's prediction. Crow's theory assumes that the flow is mature, so this delay is not surprising. Also, we have observed that vortex pairs with $Fr \geqslant 2$ have an initial adjustment period that lasts about 2 *advective* time units, $\tau \simeq 2b_0/W_0$. A similar time shift is present in the results of Spalart (1996). A lower value of Re does not appear to delay the onset of the acceleration phase of the vortex pair, but it does result in the vortex pair not accelerating as quickly or propagating as far as at higher Re.

Next, consider the implications of changing Fr. The vertical positions and separa-

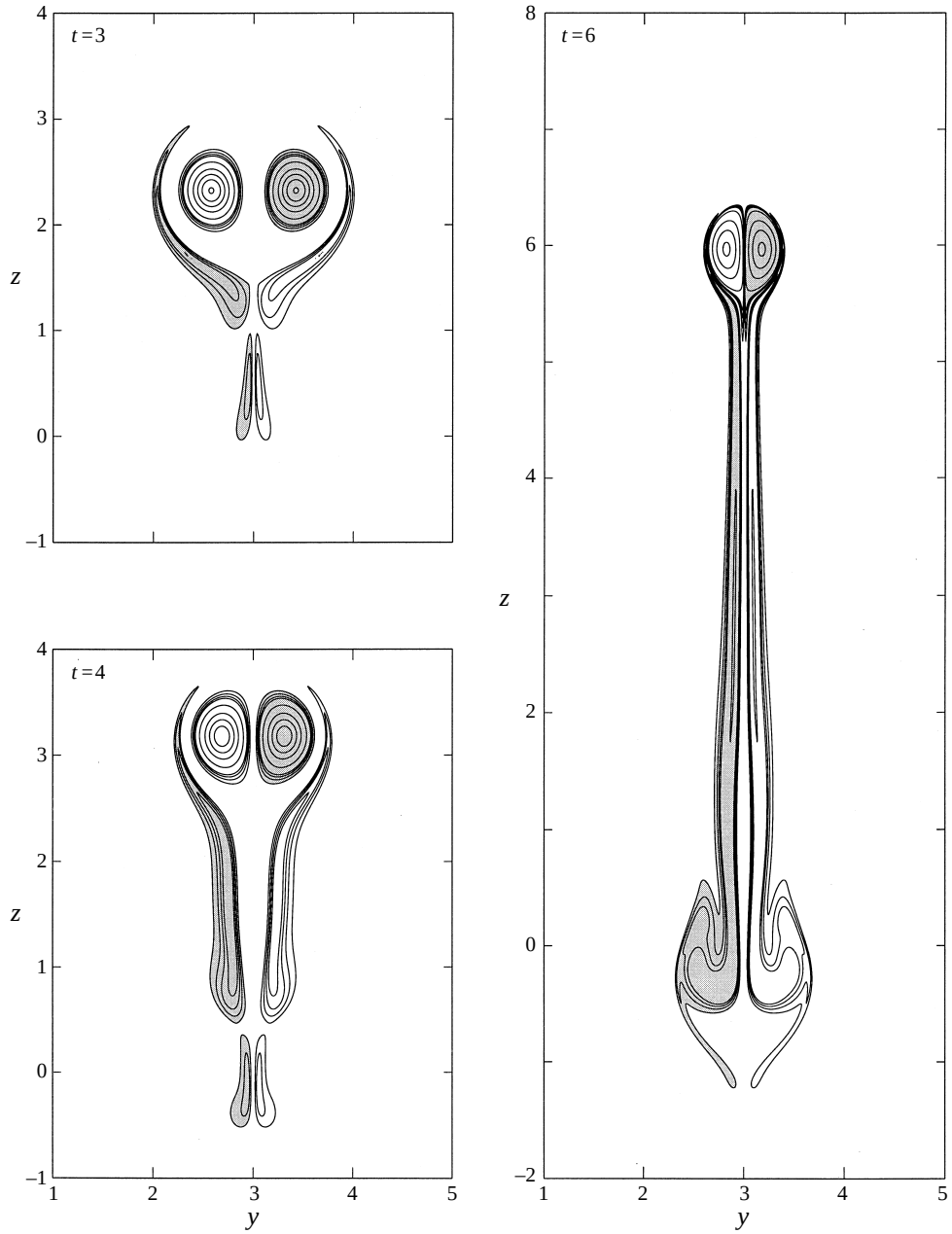

FIGURE 4. As in figure 1, but for the flow of an upwards-propagating vortex pair having $Fr = 2$ and $Re = 1500$.

tion distances of vortex pairs with different Fr but all with $Re = 1000$ are shown in figure 6, where we use re-normalized heights and times as shown. During an initial adjustment phase, which lasts roughly 2 advective time units independent of Fr, the separation distance remains fixed, and even slightly increases for the smaller values of Fr. As a constant separation distance is one of the assumptions of Saffman's theory,

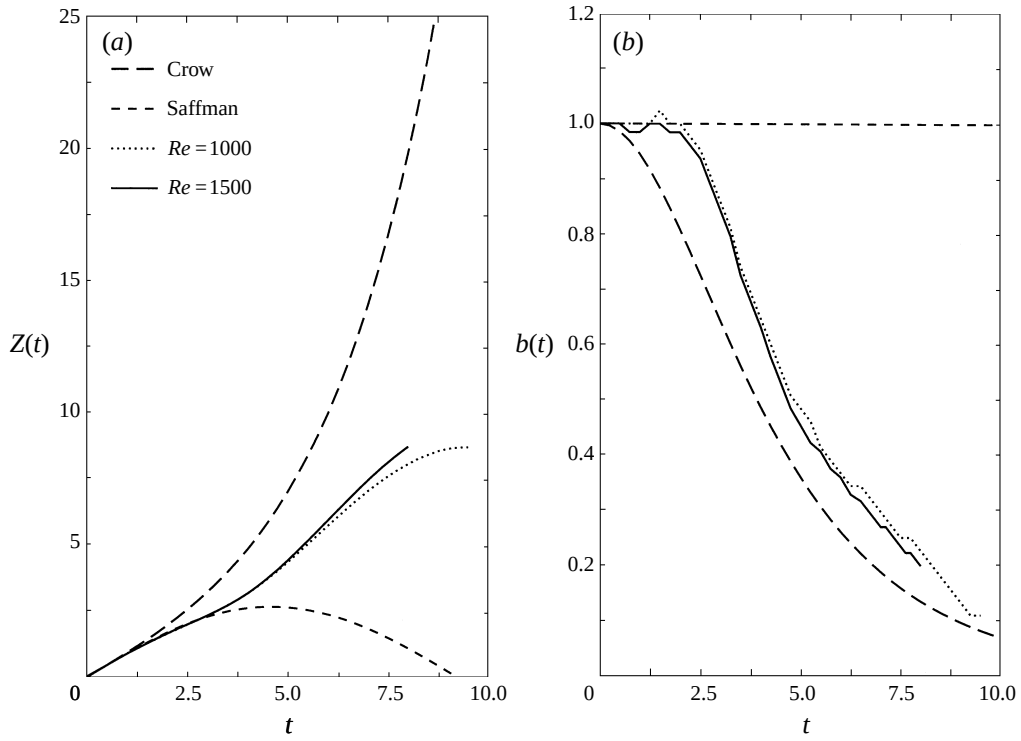

FIGURE 5. The vertical position (*a*) and the separation distance (*b*) as functions of time for vortex pairs with $Fr = 2$ and $Re = 1000$ and $Re = 1500$. The curves are compared to the expectations of the Saffman and Crow models.

it is not surprising that the vertical position follows Saffman's prediction during this adjustment phase.

After the adjustment phase (a different value of Nt for each Fr), the vortex pairs enter the acceleration phase, with a character predicted qualitatively by Crow's theory. Although Crow's theory was not intended to apply to Froude numbers as low as $Fr = 1$, it is interesting to note that the $Fr = 1$ vertical position does display acceleration. Although the agreement with Crow's predictions is better for higher Fr, this is only a consequence of the adjustment time being smaller.

Each of the vortex pairs then enters a viscous phase, where the acceleration (and also the vertical propagation) is halted at late times because diffusion decreases the circulation of the primary vortices. Crow's theory is inviscid, and so cannot predict what happens once this phase begins. The time scale on which this phase begins appears to be independent of Fr, so for example the $Fr = 8$ curve agrees less well with theory at later Nt than the $Fr = 4$ curve, because the diffusion phase for $Fr = 8$ occurs earlier in Nt units. The limitation on the duration of the acceleration phase is the fact that $b(t)$ cannot decrease indefinitely; eventually the primary vortices come close to one another and diffuse rapidly.

3.2.3. *Viscous limit on the propagation of vortex pairs*

Since the separation distance of the vortex pair decreases with time, and since each vortex simultaneously diffuses outwards, the vortices eventually come into contact and diffuse into one another, ending their acceleration phase. By calculating when

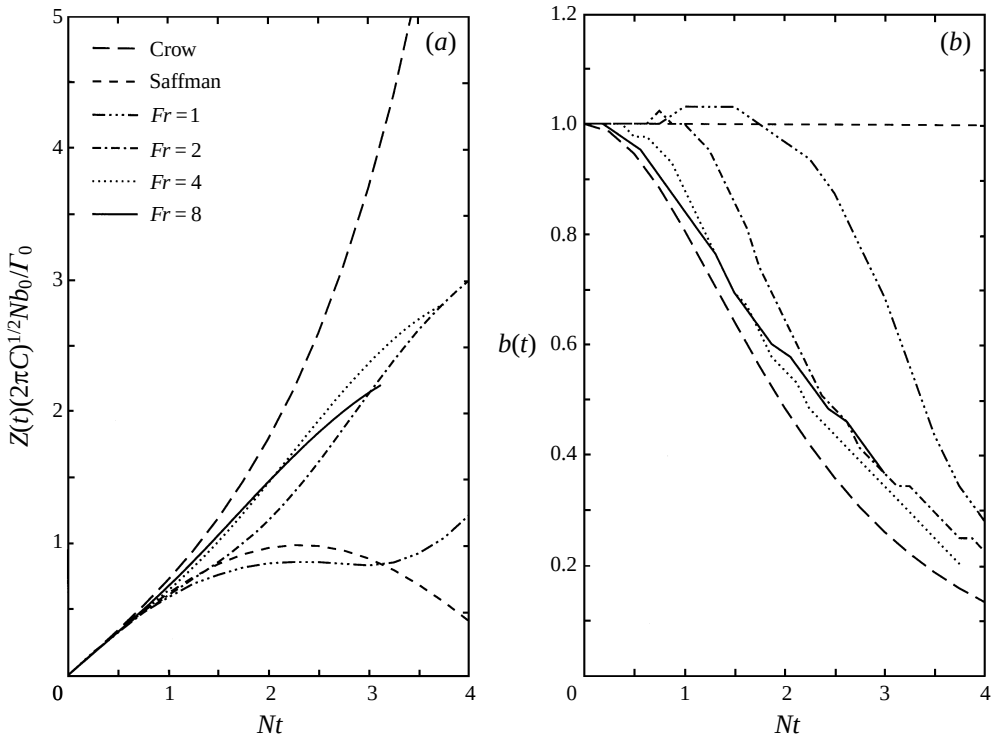

FIGURE 6. The vertical position (*a*) and the separation distance (*b*) as functions of time for vortex pairs with $Re = 1000$ and $Fr = 1$, $Fr = 2$, $Fr = 4$, and $Fr = 8$. The curves are compared to the expectations of the Saffman and Crow models.

the viscous phase begins, we can construct a rough upper limit for the total distance propagated by the vortex pair during the acceleration phase.

First, consider the outwards diffusion of each vortex. In the absence of other effects, a Gaussian vortex will self-similarly diffuse. That is, its core size will increase with time, but its total circulation and Gaussian shape will be preserved. To solve for the core size as a function of time, let $\omega = \Omega(t)\mathrm{e}^{-\rho^2/2\sigma(t)^2}$ describe a solitary vortex of fixed circulation $2\pi\Omega(0)\sigma(0)^2$. In the absence of other effects, the vorticity equation becomes

$$\frac{\partial\omega}{\partial t} = \frac{1}{Re}\nabla^2\omega. \tag{3.9}$$

This equation can be solved straightforwardly (e.g. see Lamb 1945) to yield

$$\sigma(t) = \left[\sigma(0)^2 + \frac{2}{Re}t\right]^{1/2}. \tag{3.10}$$

This solution gives a prediction for the behaviour of the vortices' core size in our simulations. The prediction is somewhat approximate as other effects lead the vortices into slightly non-Gaussian shapes (see e.g. figure 1).

The behaviour of the separation distance with time is found by combining the prediction of Crow's theory with our empirical observation of an adjustment phase of 2 advective time units. The prediction for the separation distance is then

$$b(t) = \frac{b_0}{\cosh((C/2\pi)^{1/2}N(t-2))} \quad (t > 2). \tag{3.11}$$

		Re				
	Fr	1000	1500	3000	10 000	50 000
$\sigma(0)/b_0 = 0.125$	1	4.58	4.77	5.05	5.27	5.34
	2	6.83	7.33	7.98	8.59	8.87
	4	10.5	11.7	13.3	15.1	15.8
	8	16.1	18.3	21.9	26.7	29.6
	16	23.6	27.9	35.5	47.0	55.6
$\sigma(0)/b_0 = 0.04$	1	6.12	6.87	8.22	10.8	12.8
	2	8.92	10.2	12.8	17.8	23.0
	4	13.1	15.1	19.5	28.6	40.8
	8	19.0	22.5	29.8	45.7	71.6
	16	26.9	32.7	44.3	71.2	121.0
$\sigma(0)/b_0 = 0.01$	1	6.43	7.35	9.36	14.6	25.9
	2	9.26	10.8	14.0	22.3	40.8
	4	13.5	15.8	20.8	33.6	63.4
	8	19.3	23.1	30.9	50.5	97.4
	16	27.3	33.2	45.5	75.9	148.0

TABLE 1. The predicted distance, $Z(\tau)$, that a vortex pair with given *Fr*, *Re*, and $\sigma(0)/b_0$ will propagate before the primary vortices begin to diffuse into one another. Note that these predictions are made assuming that the flow remains laminar for all time.

The vortex cores will come into contact and diffuse into one another when $2\sqrt{2}\,\sigma(\tau) = b(\tau)$. (Although σ has been used as a core size, $\sqrt{2}\,\sigma$ is a better *effective* core size in terms of how much the vortices overlap.). Thereafter, the primary vortices begin to lose their circulation, and the acceleration ceases. The value of τ must be found numerically, after which a prediction can be made for how far a vortex pair will propagate before the primary vortices begin to diffuse into one another. Including the time offset, this distance is

$$Z(\tau) = \frac{\Gamma_0}{(2\pi C)^{1/2} N b_0} \sinh((C/2\pi)^{1/2} N(\tau - 2)) + 2W_0. \tag{3.12}$$

Values of $Z(\tau)$ for different values of *Fr*, *Re*, and $\sigma(0)/b_0$ are shown in table 1. The higher values of *Re* and the smaller value of $\sigma(0)/b_0$ are included to give a sense of the variability of the results. The simple model leading to (3.12) does not include other effects such as turbulence that might prevent the vortex pair from propagating such extreme distances. Indeed, the laboratory results of Tomassian (1979) indicate that turbulent effects result in a rapid end to the acceleration phase of the vortex pair. Nonetheless, note that at the largest value of $\sigma(0)/b_0$, an increase in *Re* by as much as two orders of magnitude gives an increase in $Z(\tau)$ of only $15 - 100\%$, depending on the value of *Fr*. In our simulations, the distances that the $Fr = 2$, 4, and 8 vortex pairs with $Re = 1000$ and $\sigma(0)/b_0 = 0.125$ propagate before viscous processes begin to play a visible role (judged by the change in curvature of the trajectories displayed in figure 6) are roughly 6.4, 10.8, and 16.2 (or roughly 2.4, 2.0, and 1.5 in the re-normalized distances in figure 6), respectively. These observed values agree with the predictions shown in table 1 within a few percent.

While it is possible to predict when the acceleration phase of a vortex pair will end, and how far the vortex pair propagates by that time, it is more difficult to predict how

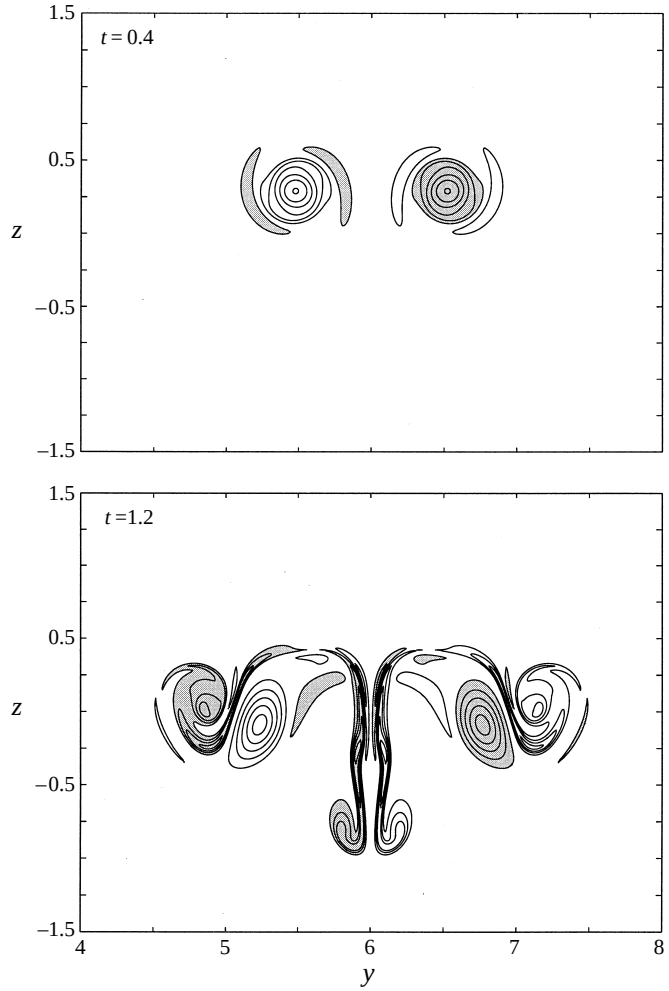

FIGURE 7. For caption see facing page.

much further the vortex pair will propagate before its progress is completely halted. This is made difficult by the possibility of instability, as will be discussed in § 4; such instabilities lead relatively quickly to the final destruction of the primary vortices.

3.3. *Flows dominated by buoyancy*

We now discuss simulations of vortex pairs in the linear regime ($Fr < 1$). For such values of Fr, buoyant processes are more important than advective processes. The evolving flow spreads out to a greater degree in the horizontal direction and exhibits smaller vertical excursions. Accordingly, the computational domain width is increased to $12b_0$ for the simulations discussed in this subsection, while the domain height is decreased to $12b_0$. We begin with the $Fr = 1/8$ case and continue with comparisons of our results with the predictions of Saffman's model.

3.3.1. *Upwards-propagating vortex pair at* $Fr = 1/8$

We first consider the evolution of an upwards-propagating vortex pair with $Fr = 1/8$ and $Re = 1000$. Contours of vorticity detailing the evolution of the

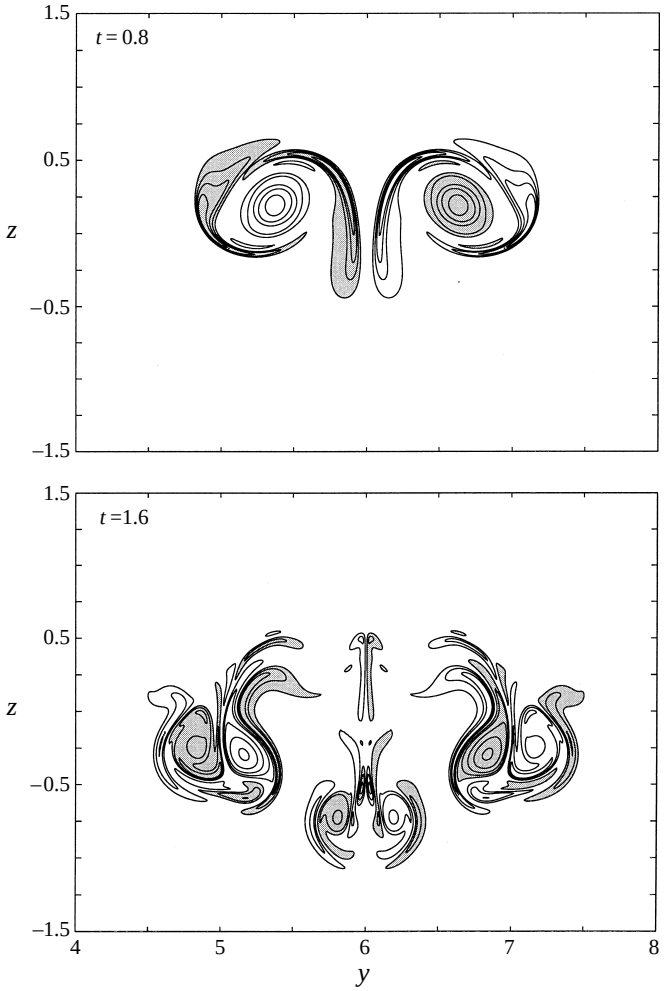

FIGURE 7. Contours of vorticity for an upwards-propagating vortex pair having $Fr = 1/8$ and $Re = 1000$. Contour levels are at $\pm 10, \pm 20, \pm 30$, etc., and all regions enclosed by negative contours are shaded.

flow through the first two buoyancy periods ($T_B = 2\pi/N = 2\pi Fr = 0.8$) are shown in figure 7. Initially, the evolution resembles that of the other vortex pairs we have discussed: counter-sign baroclinic vorticity forms around the primary vortices due to the horizontal density gradients that result from the vortices' initial flow field. However, the advective time scale is now significantly larger than the buoyancy time scale, and so the amplitude of the counter-sign vorticity grows to be competitive with the primary vortices since the locations of the baroclinic source remain in virtually fixed positions for roughly the first half of a buoyancy period ($t \simeq 0.4$). The flow field of the baroclinic vorticity prevents the initial vortex pair from advecting in the vertical direction by a significant amount and also drives the primary vortices apart during the second half of the buoyancy period. Additional vorticity forms baroclinically about these baroclinic regions of vorticity, and by the end of the second buoyancy period ($t \simeq 1.6$), the flow displays the pattern of gravity wave radiation from a localized source.

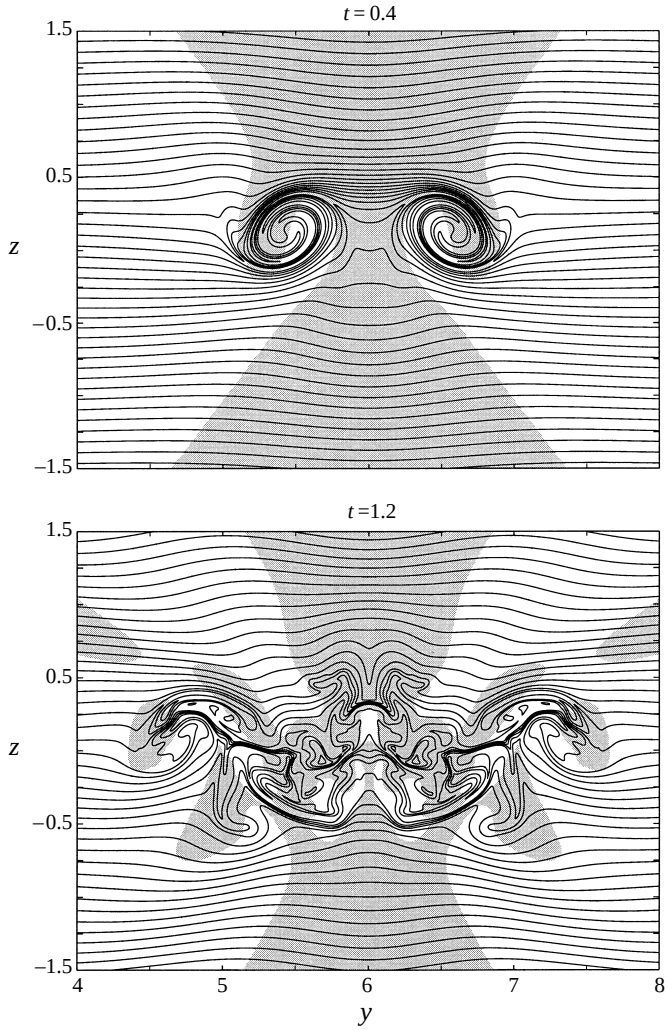

FIGURE 8. For caption see facing page.

When buoyancy dominates over advection, the fluid equations are nearly linear, and perturbations may be described in terms of linear gravity waves. The relatively heavier/lighter fluid initially displaced upwards/downwards by the flow field of the vortex pair relaxes back downwards/upwards due to buoyancy, overshooting its original position and supplying the forcing for gravity wave radiation.

Density contours describing the evolution of the flow through the first two buoyancy periods are shown in figure 8. Through the first half-buoyancy-period ($t \simeq 0.4$), there is uplifting/downwelling of heavier/lighter fluid by the flow field of the vortex pair. Thereafter, the motion reverses so that heavier/lighter fluid sinks/rises. This process, which is essentially gravity wave radiation, continues to alternate with a frequency near the buoyancy period. By the end of the second buoyancy period ($t \simeq 1.6$), the peaks and troughs of the density contours are arranged in a fan-like pattern indicating gravity wave radiation at a range of frequencies.

Since this simulation takes place in a more nearly linear regime, it is useful to consider how well the evolution is described in terms of linear gravity waves.

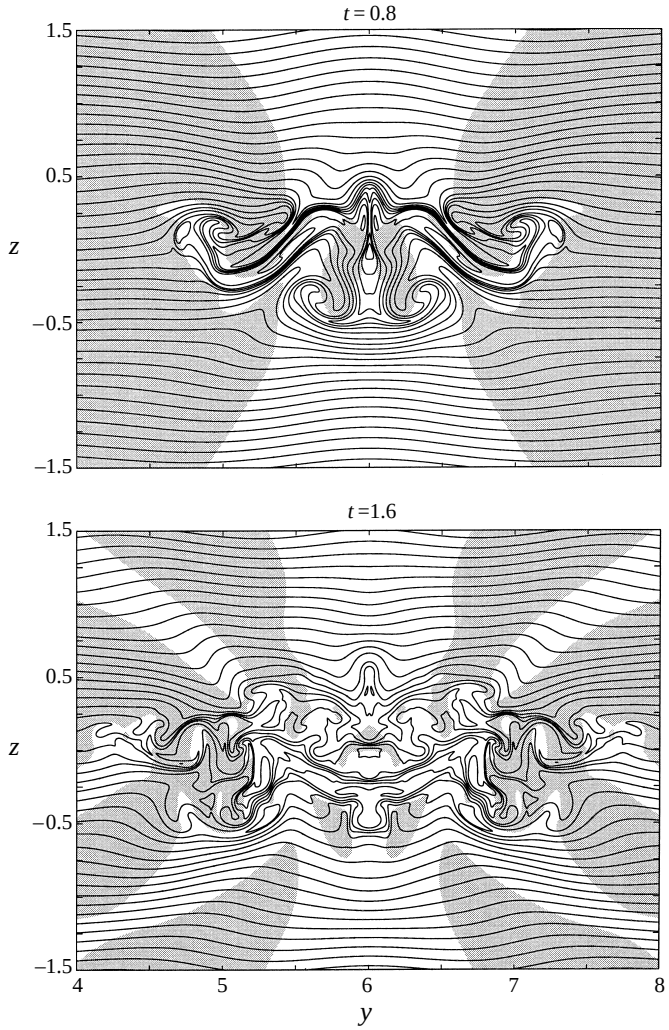

FIGURE 8. Contours of the density in the evolution of an upwards-propagating vortex pair having $Fr = 1/8$ and $Re = 1000$. The density contours have a spacing of 0.074, and all regions where the vertical velocity is negative are shaded.

Assuming that there is no mean horizontal or vertical flow, and that diffusive processes are insignificant over the buoyancy time scale, the thermal equation gives

$$\frac{\partial \rho'}{\partial t} = w' \frac{\partial \bar{\rho}}{\partial z}, \tag{3.13}$$

where variables are expanded into mean (overbar) and perturbation (primed) quantities. If the perturbation quantities ρ', v', and w' are of the form $e^{i(ky+mz-\gamma t)}$ (where γ is the frequency and k and m are the horizontal and vertical wavenumbers), then (3.13) becomes

$$\rho' = \left(\frac{-i}{\gamma} \frac{\bar{\rho} N^2}{g} \right) w'. \tag{3.14}$$

The i in (3.14) expresses the quadrature relationship between w' and ρ': the maxima (minima) of ρ' trail the maxima (minima) of w' in time by 90° of phase.

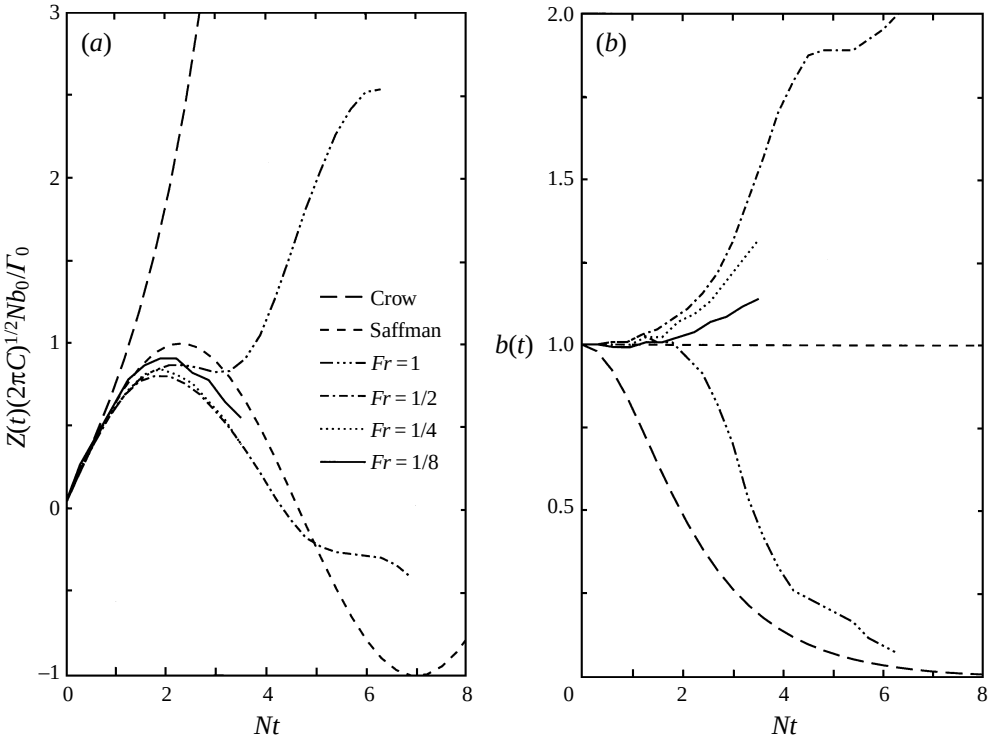

FIGURE 9. The vertical position (*a*) and the separation distance (*b*) as functions of time for vortex pairs with $Re = 1000$ and $Fr = 1$, $Fr = 1/2$, $Fr = 1/4$, and $Fr = 1/8$. The curves are compared to the expectations of the Saffman and Crow models.

Returning to figure 8, the contours of the density field are overlaid with shading where the value of the vertical velocity is negative. By the end of the second buoyancy period, the relationship between the vertical velocity and the density is in good agreement with that for linear wave propagation, apart from the smallest-scale structures near the initial vortex position. In particular, note that the region of minimum vertical velocity that is to the right of and above the initial vortex pair position is trailing (in space) the region of maximum ρ' that is centred on a line connecting the troughs of the total density. Similar correlations are also seen in the three other quadrants, implying the outward radiation of internal gravity waves excited by the initial vortex pair. At smaller Froude numbers, linear gravity wave theory will provide an increasingly accurate description of these dynamics.

3.3.2. *Other linear values of Fr and comparison to the predictions of Saffman's model*

The vertical positions and separation distances of vortex pairs with other values of Fr but all with $Re = 1000$ are shown in figure 9. To compare the different curves with each other and with the predictions of the models, re-normalized heights and time are used as before. As Fr decreases, the increasing importance of buoyancy results in an increasingly strong baroclinic source of vorticity, and in an increasingly rapid growth in circulation of the baroclinically generated regions of vorticity. Each of the trajectories in figure 9 is shown only as long as the original vortices dominate their surroundings.

First, consider the evolution of the $Fr = 1$ vortex pair. The separation distance increases only slightly during the two-advective-time-unit adjustment phase observed in the nonlinear regime. The criteria of Saffman's model are met, and so the vertical progression of the vortex pair agrees well with the model's prediction during this portion of the evolution. After roughly two advective time units, however, the separation distance decreases with time, and Saffman's model no longer applies. In this $Fr = 1$ case, the baroclinically generated regions of vorticity are sufficiently strong to advect the primary vortices together, but they are not sufficiently strong to significantly affect the vertical migration of the primary vortices. The character of the further evolution is in good agreement with the predictions of Crow's model.

Now consider the evolutions of the vortex pairs with smaller values of Fr. As before, an adjustment phase occurs, during which the separation distance of the vortex pairs remains fixed, but now the adjustment phase lasts only about 1/4 of an advective time unit, and its duration decreases (in advective time units) as Fr is decreased. As before, in re-normalized time units, the separation distance remains constant for larger Nt as the value of Fr is decreased, and also increases less sharply after the adjustment period ends.

The criteria of the Saffman model are met during this adjustment phase, and the vertical progressions of the linear regime vortex pairs are in excellent agreement with the model predictions during this time. Moreover, the character of each of the trajectories continues to be in good agreement with the prediction of Saffman's model even when the separation distance increases by as much as 50% (see the $Fr = 1/2$ curves). When the separation distance increases by more than 50%, however, the vertical progression of the vortex pair no longer agrees with Saffman's model. In this case, the vortex pair remains at a nearly constant vertical position while its separation distance continues to increase, and the long-term rebounding motion predicted by Saffman's model is not observed. The agreement with Saffman's model gets better with decreasing Fr, because the separation distance of the vortex pair increases less as Fr decreases, but the vortex pair does not dominate the flow for as long a time. Finally, the long-term rebounding motion (of the original vortices) predicted by Saffman's model does not occur.

To help understand why the separation distance of linear vortex pairs increases with time (after the end of the adjustment phase), contours of vorticity for the evolution of the $Fr = 1/4$ vortex pair during the first buoyancy period are shown in figure 10. Initially, the distributions of the two baroclinically generated regions of vorticity around each vortex are nearly symmetrically arranged. However, the two regions growing between the primary vortices quickly increase in strength to the point where they have significant advective effects on one another. By $t \simeq 0.8$ (one half of the buoyancy period), these inner regions of baroclinically generated vorticity have largely advected one another away from the primary vortices, while the regions outside the primary vortices continue to grow in strength and retain their positions relative to the primary vortices. The overall effect of these outer regions of baroclinic vorticity is to advect the primary vortices back downwards and away from one another. By $t \simeq 1.2$, these outer regions have increased in strength to the point where each of the primary vortices re-pairs with one of them, and the original vortices propagate back downwards with their separation distance increasing. The separation distance increases in this manner for all vortex pairs with initial Froude number $Fr \leqslant 1/2$, in contrast to the decreasing of the separation distance for vortex pairs with initial Froude numbers $Fr \geqslant 1$.

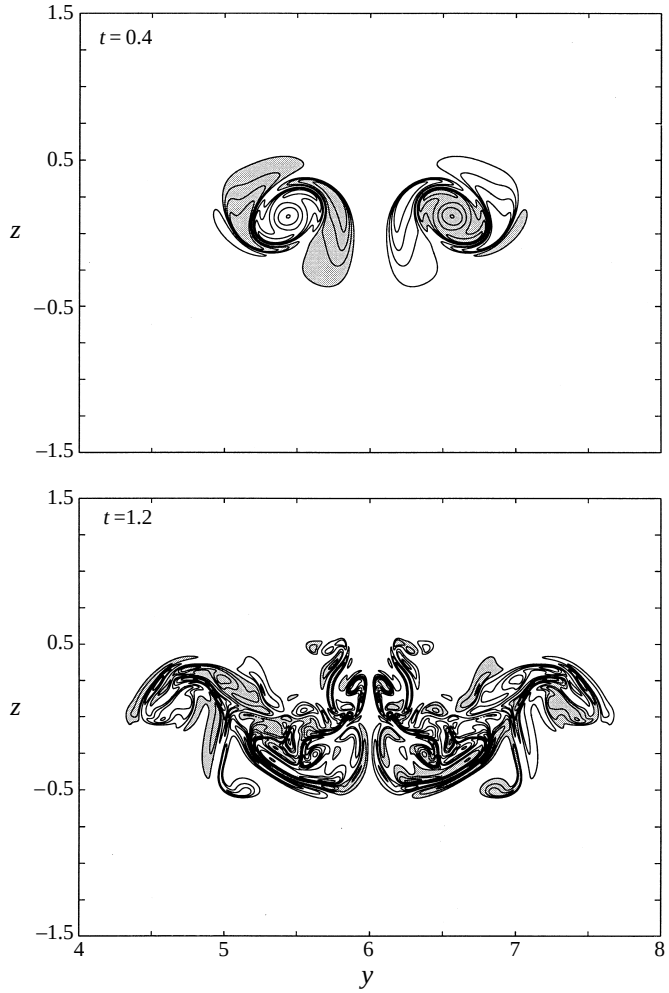

FIGURE 10. For caption see facing page.

4. Instabilities of the vortex pair and its wake

Up until now we have presented results for initial conditions with strict symmetry about the centreline. Since the equations of motion admit and conserve this symmetry, these solutions represent only a subset of the possible flow evolutions. We now discuss results in which asymmetry is introduced to the flow by the perturbations described in § 2.2. Two distinct instabilities occur: one of the jet of fluid comprising the baroclinically generated wake of the vortex pair, and one of the primary vortices themselves. Although numerical constraints currently prevent the simulation of a turbulent vortex pair, these results hint at how the evolution of a vortex pair might be different in a more realistic turbulent fluid.

4.1. *Instability of the vortex pair*

We first consider the instability of the primary vortex pair, the 'vortex head instability', which is manifested in a sinuous propagation path of the vortex pair. Figure 11 displays contours of vorticity for the case $Fr = 2$ and $Re = 1000$, where asymmetry is seeded in the initial condition. By $t = 9$, the evolution is quite distinct from the

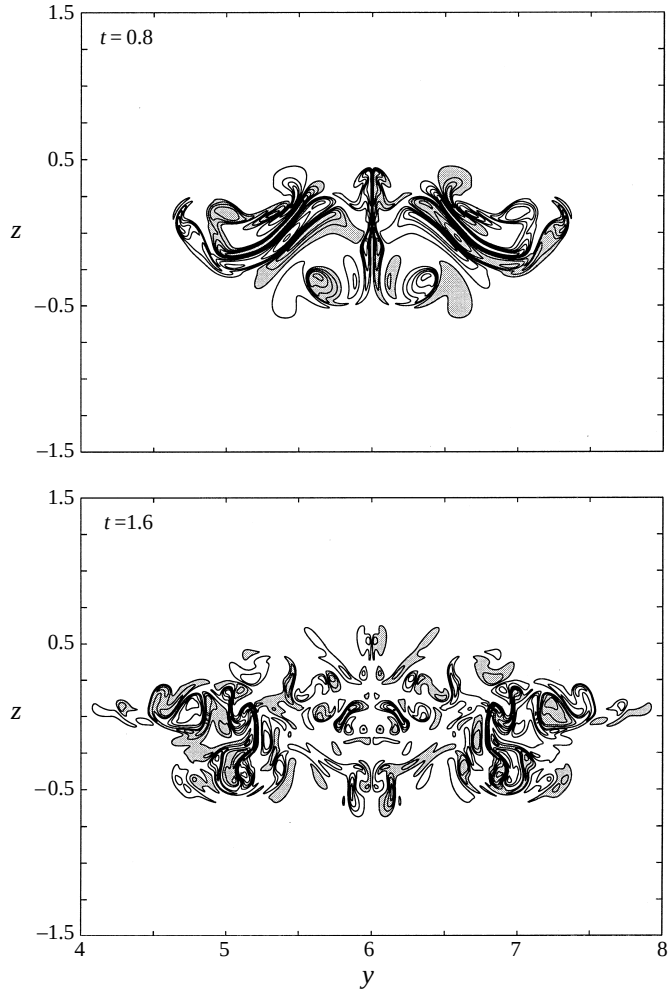

FIGURE 10. Contours of vorticity for an upwards-propagating vortex pair having $Fr = 1/4$ and $Re = 1000$. Contour levels at $\pm 10, \pm 20, \pm 30$, etc. show the distribution of high-magnitude vorticity, while additional contour levels at $\pm 2, \pm 3, \pm 4$ and ± 5 illustrate the distribution of low-magnitude vorticity, and all regions enclosed by negative contours are shaded.

symmetric case (see figure 3). The vortices deviate from their straight upwards path into a sinusoidal motion of growing amplitude. The vortex sheets comprising the baroclinically generated wake detrain from the vortex pair in the same pattern, and vortex sheet dynamics amplify their sinusoidal perturbation. Note that organized vorticity remains near the maximum height attained by the vortex pair as late as $t = 15$, in contrast to the symmetric case.

We examine this instability by studying one of its early iterations. Figure 12 shows a magnification of the region containing the vortex pair for times from $t = 6.75$ to $t = 8.25$. Note the change in structure of the vortices as time progresses. At $t = 6.75$ and $t = 7.25$ more vorticity is being detrained from the negative vortex than from the positive vortex (visible in the middle of the wake just behind the vortex pair). Also, at $t = 7.25$, the negative vortex is slightly weaker than the positive vortex, and the vortex pair rotates about the positive vortex because of this unequal strength (note the

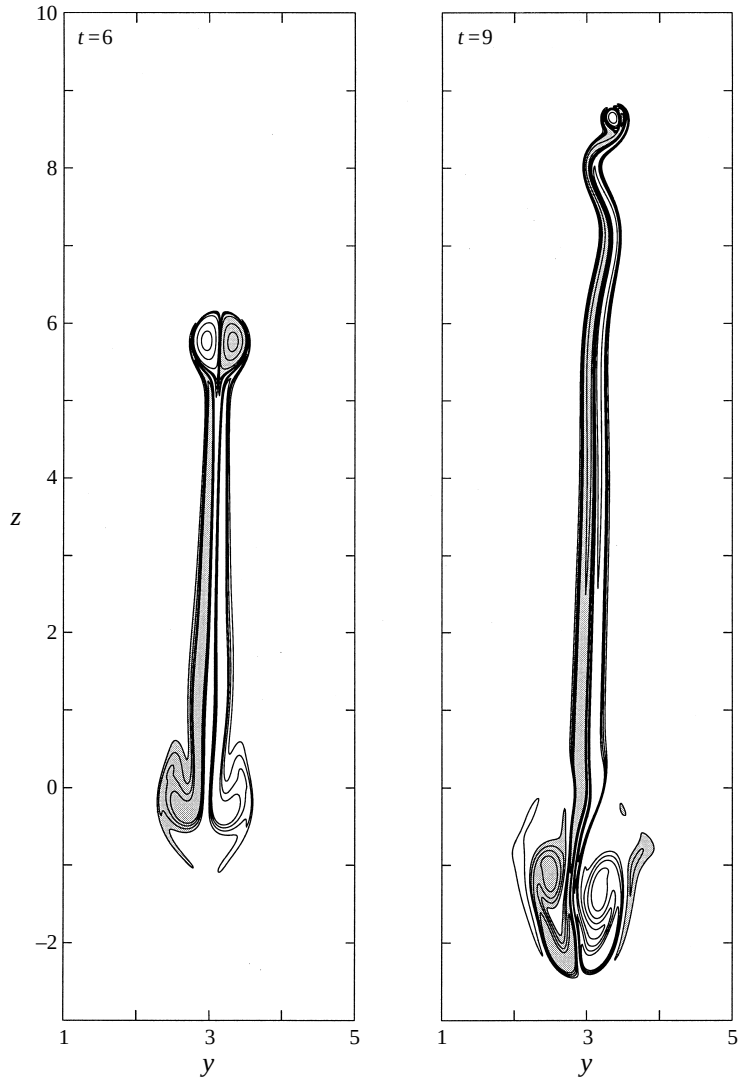

FIGURE 11. For caption see facing page.

very slight curve of the path). At $t = 7.75$, the positive vortex is being preferentially detrained into the wake; it is also weaker than the negative vortex and the pair's path curves in the other direction (see the path at $t = 8.25$). Finally, at $t = 8.25$ the detrainment again reverses, and more vorticity is being detrained from the negative vortex than from the positive vortex. As the evolution proceeds after $t = 8.25$, the amplitude of the oscillation increases and the wavelength decreases, possibly because of the decreasing circulation of the primary vortices.

Evidence of this instability appears to be present in the results of Schilling *et al.* (1996). Note in their figure 4 *e*, the sheared state of the positive vortex and the fact that the negative vortex is stronger and is apparently rotating the pair's orientation. The instability does not appear in the cases shown by Robins & Delisi (1990) or by Spalart (1996), due to the symmetry assumptions made in each case. To our knowledge, this instability has also not been observed in two-dimensional laboratory experiments,

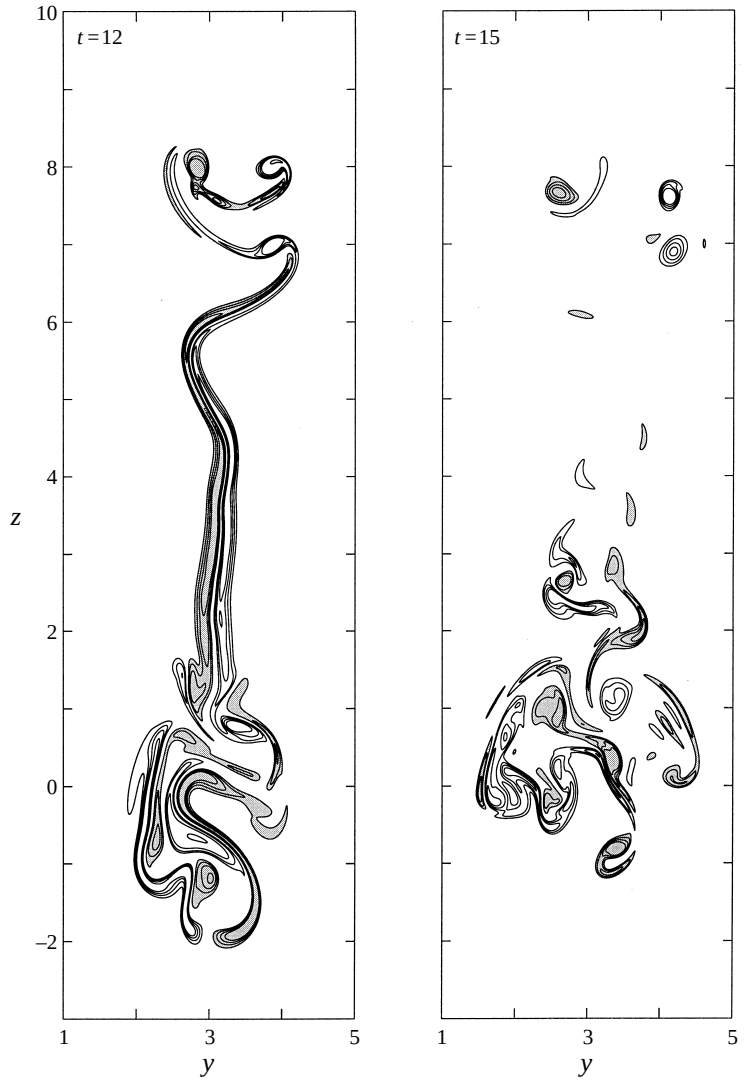

FIGURE 11. As in figure 1, but for the case in which an asymmetric perturbation is seeded in the initial conditions.

although it is not clear why. In unsheared fluids, the vortex head instability does not develop until the vortices have diffused sufficiently for their circulation to be detrained into the baroclinically generated wake. Such a process takes longer at the higher values of *Re* in laboratory experiments so that other processes may complicate the flow before the vortex head instability can begin. Another possible explanation lies in the difficulty of observing the flow's perturbations. In particular, it is difficult to observe the weak secondary vorticity with current particle image velocimetry (PIV) techniques (Fincham & Spedding 1997).

In our simulations, the vortex pair does not survive coherently for more than one or two repetitions of the instability oscillation after it has reached a visible amplitude. Eventually one of the vortices is weakened to the point where it becomes too sheared out by the flow of the wake and the other vortex to recover (in our case, by $t \simeq 8.5$,

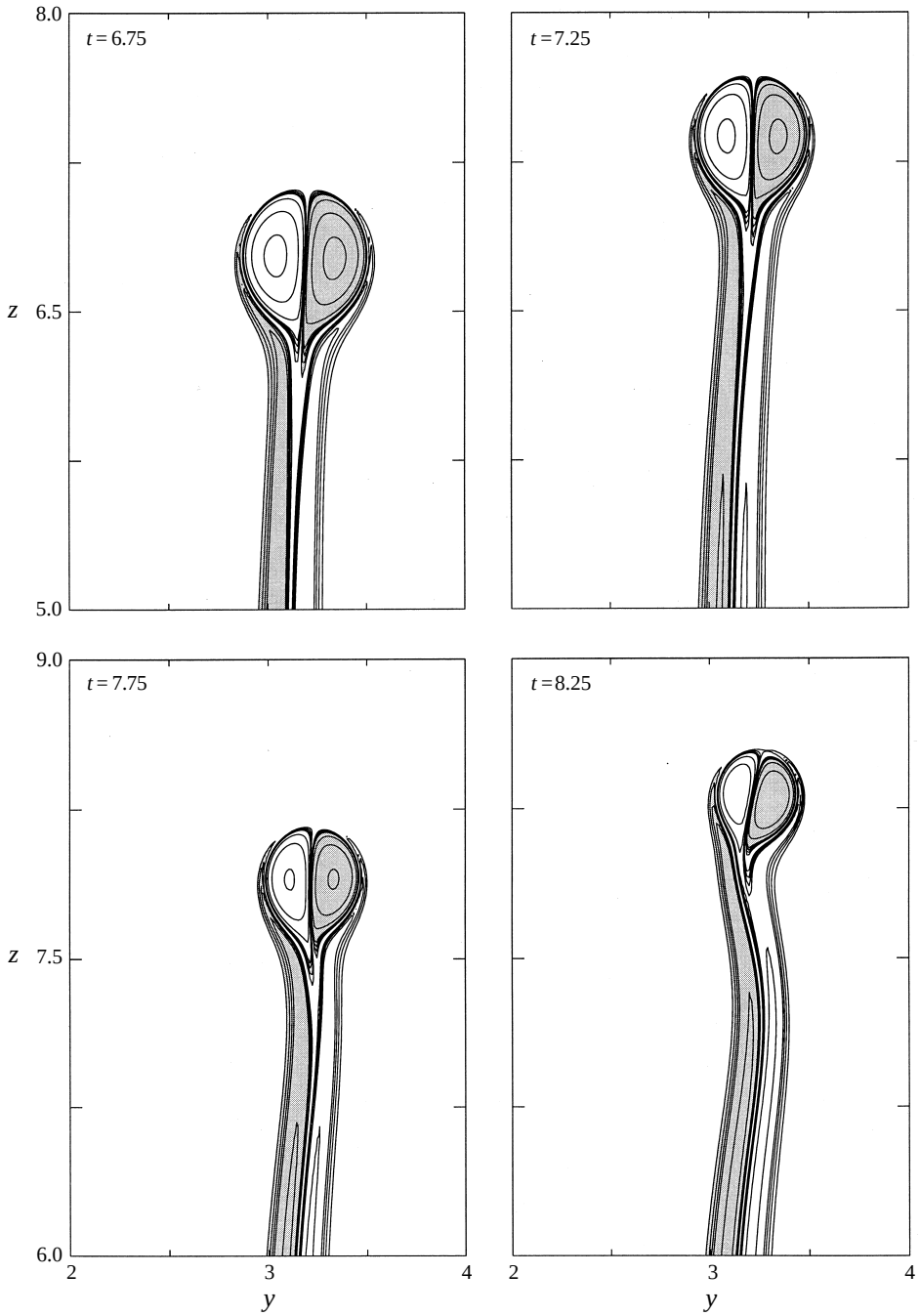

FIGURE 12. As in figure 1, with a more magnified view of the evolution of the vortex pair as it undergoes the vortex head instability.

the negative primary vortex is severely depleted, leading to the rotation seen at $t = 9$ in figure 11). The remaining vorticity is sufficiently weak that it is advected by the baroclinically generated wake vorticity in complicated ways. Generally, all of the initial primary vorticity is either detrained downwards with the baroclinically

generated wake, or combines locally with the secondary vorticity. In particular, none of the regions of vorticity near $z = 7$ at $t = 15$ in Fig. 11 are solely remnants of the primary vortices.

During the instability, the baroclinically generated vortex sheets roll up where they are the most strained (e.g. the positive roll of vorticity forming near $z = 7$ at $t = 12$ in figure 11). The additional vortices that form in this manner generally detach themselves from the downwards motion of the baroclinic jet, and move in ways that are difficult to predict. Since the baroclinic source of vorticity becomes larger the further the vortex pair propagates, the vortices forming near the top of the baroclinically generated sheets of vorticity are the strongest. These vortices interact with the vortices formed from the last interactions of the primary vortices and the local secondary vorticity, leading to a complex flow near the maximum propagation distance of the vortex pair. The continued presence of concentrated vorticity near this location is in contrast to the symmetric case (see figure 3).

The vortex pair is not susceptible to the vortex head instability until the vortices have diffused sufficiently for their circulation to be detrained. In § 3.2.3 we derived an approximate value for the distance a vortex pair propagates before this occurs. While undergoing the instability, the vortex pair spends a good deal of time propagating horizontally, and so it does not propagate as far vertically as it would if it had not undergone the instability. Therefore, this instability strongly limits how much further the weakening primary vortex pair will propagate after the viscous time scale is reached. At the same time, it leads to the formation of a complex flow that remains near the maximum height attained by the vortex pair and spreads out horizontally.

Finally, we consider the effect on the vortex head instability of changing Fr and/or Re. Contours of vorticity summarizing the evolution of a vortex pair with $Fr = 2$ and $Re = 1500$ are shown in figure 14 in § 4.2. At this higher value of Re, the more concentrated sheets of baroclinically-generated wake vorticity (see figure 4) result in the vortex head instability reaching a visible amplitude more quickly, and consequently reaching a 'saturation' amplitude more quickly (at which point the primary vortices detach from the wake vorticity). Close examination of the vorticity contours reveals that the primary vortices retain more of their circulation after this occurs than in the lower-Re case, and that the vortices which form from the strained vortex sheets also contain more vorticity at this higher Re. The additional vorticity contained in the vortices near the maximum height attained by the vortex pair results in an increasingly complex flow with increasing Re. Changing the value of Fr (within the nonlinear regime) affects the time scale of the instability. At higher Fr, the baroclinic source of vorticity is weaker, and the strength of the baroclinically generated wake vorticity is less; their weaker strength results in slower growth of the instability.

4.2. *Instability of the jet wake*

The baroclinically generated wake of a vortex pair is also susceptible to a jet instability. The flow in the wake is a vertical jet of fluid, an average profile of which is shown in figure 13 for the case $Fr = 2$ and $Re = 1500$. The profile is slightly asymmetrical because an asymmetry is seeded in the initial condition. The vertical velocity of a similar jet of fluid, the Bickley jet, with profile

$$W(y) = -A\,\mathrm{sech}^2[D(y - c)] + B, \tag{4.1}$$

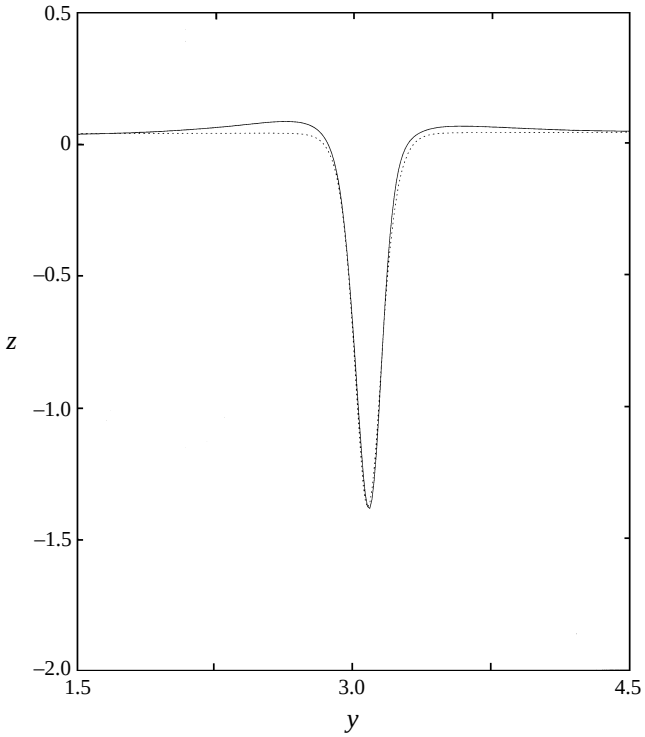

FIGURE 13. The solid line shows the average vertical velocity of the baroclinically generated wake (for the case $Fr = 2$ and $Re = 1500$, with an asymmetric perturbation in the initial conditions) at $t = 9$. The dotted line shows the Bickley jet with a velocity profile given by $w = -1.42\,\mathrm{sech}^2(10(y - 3.083)) + 0.04$.

and with $A = 1.42$, $D = 10$, $c = 3.083$, and $B = 0.04$ is also shown in figure 13. Ignoring gravity, viscosity, and the finite vertical extent of this jet, the growth periods (e-folding time scales) for the sinuous and varicose modes of instability of the Bickley jet are given by Drazin & Howard (1966). The fastest growing sinuous mode has a wavelength $\lambda_S = 6.98/D$ and a growth period $T_S = 6.21/(AD)$, and the fastest growing varicose mode has a wavelength $\lambda_V = 12.6/D$ and a growth period $T_V = 21.7/(AD)$.

Contours of vorticity spanning the time during which a sinuous mode instability develops and grows to a critical amplitude are shown in figure 14. At $t = 9$ the jet is quasi-uniform from $z \simeq 1$–6, but the instability gains a discernible amplitude by $t = 10$ and leads to a separated, complex flow by $t = 11$. The observed wavelength of this instability is 0.6, while the theory predicts the fastest growing sinuous mode to have a wavelength $\lambda_S = 0.7$ and a growth period $T_S = 0.44$. The wavelength and growth period of the observations and theory agree to within roughly 15%. As the value of Re is increased (within numerically attainable bounds), the observed wavelength and growth period of this instability remain nearly fixed, while the theoretical predictions change because the parameters A and D in (4.1) required to fit the jet change. The parameterization changes because the increasing Re results in an increasingly narrow jet with an increasingly large peak velocity. The change in A and D results in the wavelength and growth period predicted by the theory decreasing so that the simulations and the theory agree even better. This is not surprising as the theory is inviscid and is more accurate at high Re. If Re were increased further,

we expect that the thickness of this jet of fluid would continue to decrease, so that both the growth period and the wavelength would decrease, leading to a more rapidly emerging and more complex flow in the baroclinically generated wake of the vortex pair.

Note that the theory predicts a growth rate over three times slower for the fastest growing varicose mode of instability. As a general flow will have both symmetric and antisymmetric perturbations, the sinuous mode of instability will generally appear rather than the varicose mode. We have not observed the occurrence of a varicose mode of instability (at *Re* which are numerically attainable), even when the initial conditions have been seeded with only symmetric perturbations (see Garten 1997 for further discussion on this point).

5. Shear effects

We now consider counter-rotating vortex pairs in stratified and sheared environments. We take the mean shear to have uniform slope throughout the region of interest, and to be parameterized by the Richardson number, *Ri*, as defined in § 2.2 ($V(z) = NRi^{-1/2}(z - L_z/2)$). In what follows, the vortex with the same (opposite) sign of vorticity as the mean shear will be called the same-sign (opposite-sign) vortex, and is also known in the literature (see e.g. Lissaman *et al.* 1973) as the downstream (upstream) vortex. A trivial effect of the mean shear is to advect the vortex pair horizontally as it propagates vertically. A more subtle effect is that the opposite-sign vortex loses its circulation more quickly than the same-sign vortex due to viscous diffusion and detrainment of vorticity. The vortex pair then rotates with the same rotational sense as the mean shear. The additional presence of stratification can cause the vortex pair to rotate earlier in its evolution, and with a rotational sense opposite that of the shear flow, an effect that is intimately connected to the asymmetric distribution of the flow's streamlines. This earlier rotation of the vortex pair can result in a solitary vortex emerging more quickly than in the unstratified case.

5.1. *Review of theory*

Lissaman *et al.* (1973) have presented a theory for the effect of a uniform shear on the motion of a vortex pair, which we re-state here in a slightly different form. It relies on the asymmetric distribution of the flow's streamlines.

Consider the initial distribution of streamlines for a counter-rotating vortex pair with a mean shear, in the reference frame moving with the vortex pair. Defining the streamfunction $\psi(y, z)$ such that $v = \partial\psi/\partial z$ and $w = -\partial\psi/\partial y$, we integrate (2.9) to obtain

$$\psi(y, z, t = 0) = \sigma^2\omega_0\left[\ln\left(\frac{r_2}{r_1}\right) + \mathrm{Ei}\left(\frac{-r_1^2}{2\sigma^2}\right) - \mathrm{Ei}\left(\frac{-r_2^2}{2\sigma^2}\right)\right] + W_0 y + \frac{1}{2}\left(\frac{\partial V}{\partial z}\right) z^2, \quad (5.1)$$

where $r_1 = [(y - y_1)^2 + (z - z_1)^2]^{1/2}$, $r_2 = [(y - y_2)^2 + (z - z_2)^2]^{1/2}$, and $\mathrm{Ei}(x)$ is the exponential integral (Abramowitz & Stegun 1964). The first term on the right-hand side of (5.1) is the velocity field of the vortex pair itself†, the second term is due to the shift to the moving reference frame of the vortex pair, and the third term is the additional contribution of the mean shear flow (where $\partial V/\partial z$ is assumed to be constant).

† To a very good approximation, the streamfunction for a pair of point vortices may be substituted for this streamfunction.

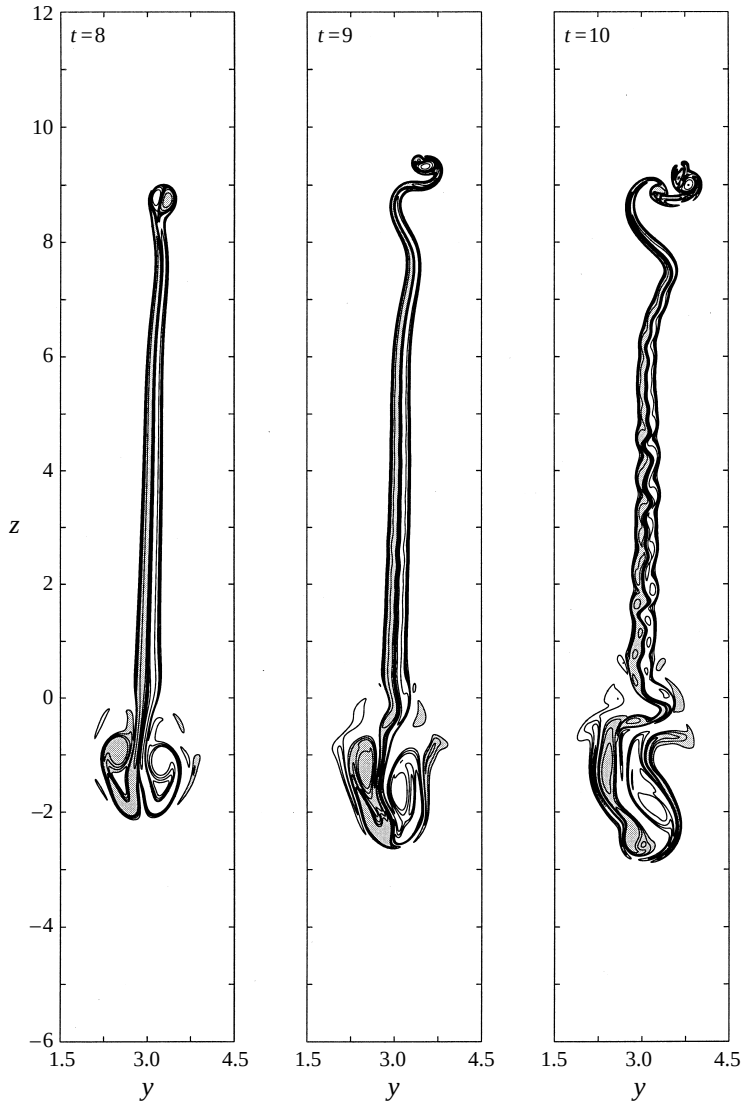

FIGURE 14. For caption see facing page.

Contours of the streamfunction for an upwards-propagating vortex pair with no mean shear are shown in figure 15(*a*). The streamline that separates the closed streamlines from the open streamlines is called the separatrix. Apart from diffusion, fluid within the separatrix is carried with the vortex pair (within the two re-circulation cells), while the fluid outside the separatrix is not. As the vortex pair evolves, the streamfunction changes somewhat, but the overall characteristics of the streamlines remain.

Contours of the streamfunction for an upwards-propagating vortex pair with mean shear given by $\partial V/\partial z = 1/2$ (corresponding to $Fr = 2$ and $Ri = 1$) are shown in figure 15(*b*). An asymmetry is apparent in these streamlines: the re-circulation cell of the (left-hand) opposite-sign vortex is smaller than in the unsheared case, and the re-circulation cell of the (right-hand) same-sign vortex is larger than in the unsheared

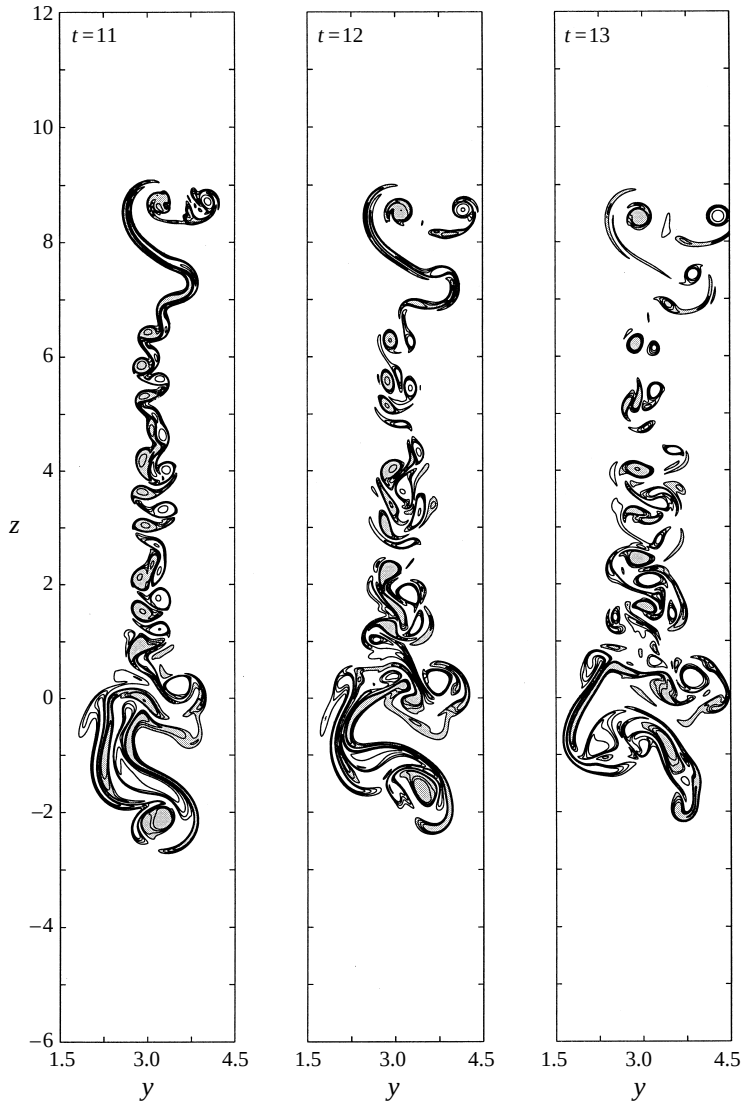

FIGURE 14. As in figure 4, but for the case in which an asymmetric perturbation is seeded in the initial conditions.

case. The vortices will diffuse outwards as they advect upward, and even though the rates of diffusion are the same, the opposite-sign vortex will diffuse to the boundary of its smaller re-circulation cell more quickly than the same-sign vortex. When that occurs, some of the vorticity of the opposite-sign vortex will be detrained, and the opposite-sign vortex will become weaker than the same-sign vortex. The opposite-sign vortex, being weaker, will then rotate about the same-sign vortex, with the same rotational sense as the background shear flow.

5.2. *Upwards-propagating vortex pair in an unstratified fluid with* $\partial V/\partial z = 1/2$

We first consider the evolution of an upwards-propagating vortex pair in a sheared, constant-density fluid, with $Re = 1000$. The orientation of the shear is defined such that the horizontal velocity increases to the right with height ($\partial V/\partial z > 0$); therefore,

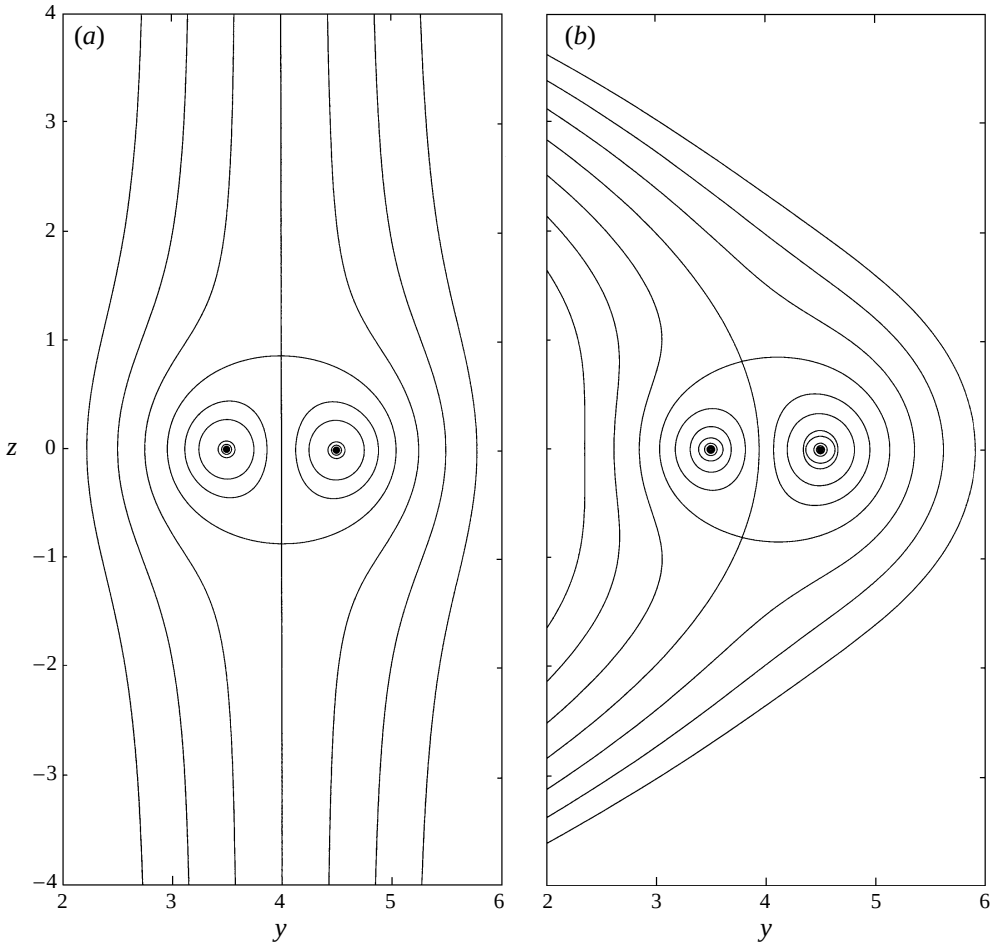

FIGURE 15. Streamlines of a counter-rotating vortex pair having $Fr = 2$ in (*a*) the unsheared and (*b*) sheared ($Ri = 1$) cases. In the sheared case, the background shear flow is defined such that the horizontal velocity increases to the right with height. Note that the streamlines are shown in the moving reference frame of the vortex pair.

the vorticity of the left (right-hand) vortex has the opposite (same) sign of vorticity as the background shear.

Contours of vorticity for the evolution are shown in figure 16. Here, as in all subsequent plots of sheared evolutions, the horizontal advection of the vortex pair by the shear is subtracted to give a common frame of reference. At early times, the vortex pair propagates upward in a straight line. However, by $t \simeq 8$, the vortices have diffused outwards sufficiently to encounter the boundaries of their re-circulation cells. The opposite-sign vortex diffuses outwards to the boundaries of its smaller re-circulation cell faster than the same-sign vortex, and so more of its circulation is detrained behind the vortex pair (too small to see in the contours shown).

By $t \simeq 16$, this asymmetry in the strength of the vortices results in the stronger same-sign vortex rotating the weaker opposite-sign vortex about itself, while the vortices continue their upward propagation. At later times, the vorticity of the opposite-sign vortex becomes more spread out (see $t = 20$). The flow then evolves to where the

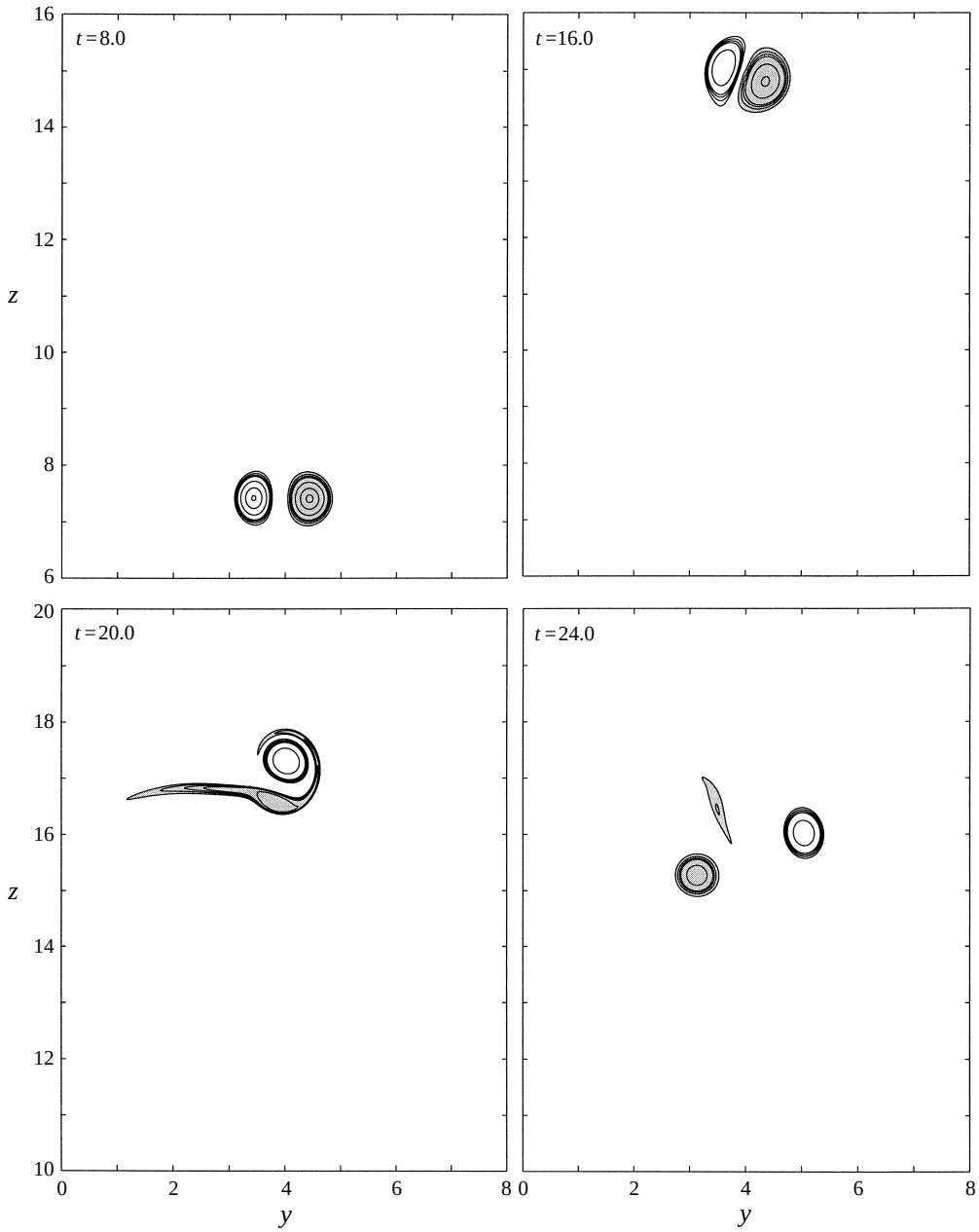

FIGURE 16. Contours of vorticity for an upwards-propagating vortex pair in an unstratified, sheared ($\partial V/\partial z = 1/2$) fluid, with $Re = 1000$. Contour levels at $\pm 10, \pm 20, \pm 30$, etc. show the distribution of high-magnitude vorticity, while contour levels at $\pm 2, \pm 3, \pm 4$ and ± 5 illustrate the distribution of low-magnitude vorticity, and all regions enclosed by negative contours are shaded. The vorticity at each time has been shifted in the horizontal direction to the centre of the domain.

vortices are again of almost equal strength (see $t = 24$). However, they are further apart than their initial separation distance, their mutual advection is no longer purely in the vertical direction, and some excess negative vorticity has been detrained. Thus, we find that the rotation of the vortex pair in an unstratified, sheared fluid does not

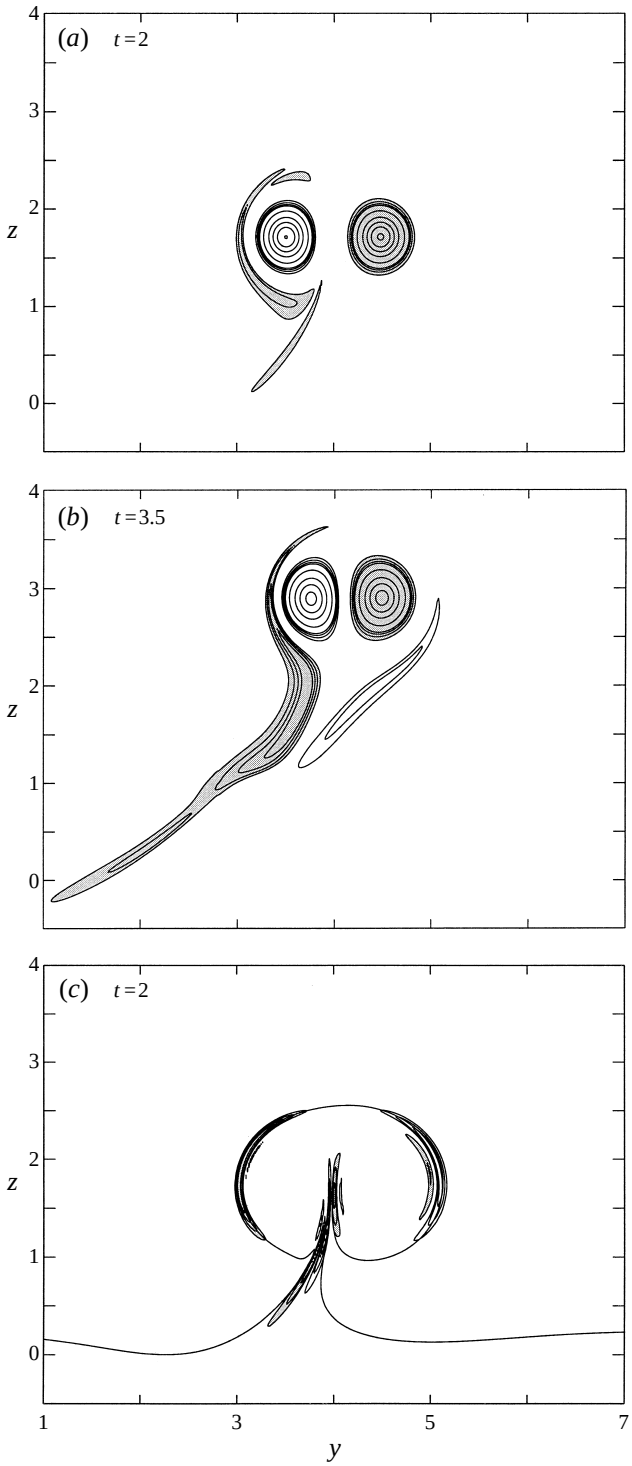

FIGURE 17(*a*, *b*, *c*). For caption see facing page.

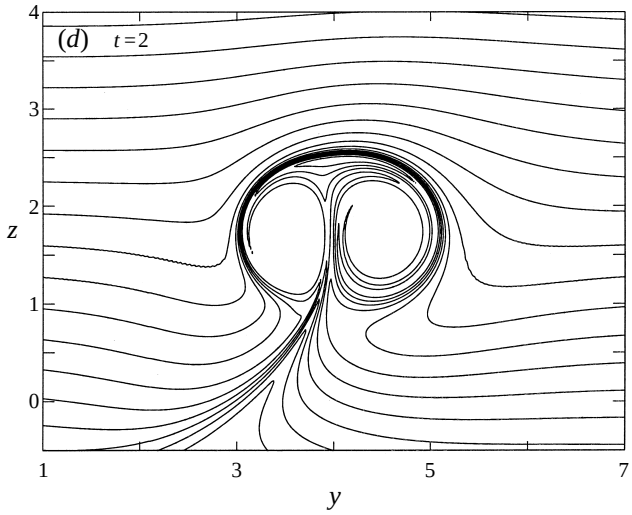

FIGURE 17(*d*). Contours of (*a*, *b*) vorticity, (*c*) the baroclinic source of vorticity, and (*d*) density for an upwards-propagating vortex pair with $Fr = 2$, $Ri = 1$, and $Re = 1000$. The quantities are shifted in the horizontal direction for display purposes. Primary contour levels of the vorticity are at intervals of 10, though the zero-line is not shown. Additional contour levels are shown at $\pm 2, \pm 3, \pm 4$ and ± 5 to illustrate the distribution of vorticity with lower magnitudes, and all regions enclosed by negative contours are shaded. The contour levels of the baroclinic source are the same as for the vorticity, while the contour levels of the density are at intervals of 0.296.

occur until after a viscous time scale has been reached, and that a solitary vortex does not emerge after several multiples of this time scale.

A comparison of the distribution of the vorticity at times $t = 20$ and $t = 24$ shows the hazard of determining the character of the evolution of a sheared vortex pair by only considering widely spaced times. If the distribution of vorticity were only considered at $t = 20$, then one might conclude that the opposite-sign vortex is stronger than the same-sign vortex, and is dominating the evolution of the flow. However, by considering nearby times in the evolution (e.g. $t = 24$), this interpretation is shown to be incorrect.

5.3. *Upwards-propagating vortex pair with $Fr = 2$ and $Ri = 1$*

We now consider the evolution of an upwards-propagating vortex pair with $Fr = 2$ and $Ri = 1$ (with the same mean shear as in the unstratified case). Here again the left (right)-hand vortex will be referred to as the opposite-sign (same-sign) vortex. Contours of vorticity detailing the early evolution of the vortex pair are shown in figure 17 (*a*, *b*). In the presence of both stratification and mean shear, an asymmetry in the distribution of vorticity begins to appear quickly ($t \simeq 2$) and grows with time in both magnitude and extent.

To determine the cause of this asymmetry, the contours of the baroclinic source of vorticity are shown in figure 17 (*c*). Relatively more negative vorticity (contour levels -2, -3, -4, -5) is generated around the left-hand positive vortex than positive vorticity (contour levels $+2$, $+3$, $+4$) around the right-hand negative vortex. This asymmetry in the baroclinic source results from an asymmetry in the horizontal density gradients. The horizontal gradient of density to the left of the positive vortex

is stronger than that to the right of the negative vortex, as shown by the closer packing of density contours in figure 17 (*d*).

The closer packing of density contours on one side of the vortex pair is a result of faster advection by the flow field. To understand this, we return to the streamlines of the initial Gaussian vortex pair in the imposed mean shear shown in figure 15 (*b*). The vertical velocity of this flow is symmetric about the centre of the vortex pair (since the additional flow due to the mean shear is strictly horizontal). However, since the separatrix is not symmetric about the centre of the vortex pair, the vertical velocities on the left- and right-sides of the separatrix are different. In particular, the magnitude of the vertical velocity at the separatrix is larger on the left-hand side of the vortex pair. As shown in figure 17 (*d*), this larger vertical velocity wraps density contours more closely together about the (left-hand) opposite-sign vortex, which in turn leads to the greater baroclinic production of vorticity to the left of the vortex pair, as shown in figure 17 (*c*). This asymmetry in the baroclinic source of vorticity occurs for all *Fr* and *Ri*.

The advective effects of the asymmetric vorticity distribution cause the primary vortices to tilt with a sense opposite to the rotation of the mean shear. Specifically, the counter-clockwise flow field of the stronger negative vorticity to the left of and below the (left-hand) opposite-sign primary vortex suppresses the upward motion of the opposite-sign vortex relative to that of the (right-hand) same-sign primary vortex. This tilting is difficult to discern, but at $t = 3.5$ (figure 17 *b*) the (right-hand) same-sign vortex is slightly higher than the (left-hand) opposite-sign vortex.

Contours of vorticity at more advanced times are shown in figure 18, illustrating that the tilting is only temporary. At $t = 5.0$, the (left-hand) opposite-sign vortex has been weakened relative to the same-sign vortex; the advective effects of the asymmetric, baroclinically generated wake vorticity have spread out the (left-hand) opposite-sign vortex (seen in the wake right behind the vortex pair). The (right-hand) same-sign vortex is then stronger than the (left-hand) opposite-sign vortex, so that the vortices now tilt with the same rotational sense as the mean shear. By $t = 6.0$, however, the (right-hand) same-sign vortex has been preferentially detrained, and the direction of tilting again reverses.

This process has the same morphology as the vortex head instability discussed in § 4.1 (compare figure 18 to figure 12), and as before the process does not survive many iterations once it becomes visible. However, this evolution departs from the unsheared case in that the instability appears sooner and proceeds at a faster rate, due apparently to the asymmetry present at early times. The initial asymmetry also apparently results in the vortex pair surviving a smaller number of iterations of the instability and in the vortex pair separating from the wake vorticity. When the vortex pair separates, the same-sign vortex is slightly stronger than the opposite-sign vortex, so the opposite-sign vortex rotates around the same-sign vortex in the same sense as the rotation of the mean shear. The vortex pair continues to rotate in this direction and intersects the baroclinic wake; at $t = 10.0$, the major portion of remaining concentrated opposite-sign vorticity is actually from the baroclinically generated wake vorticity. At this point, one might say that a solitary vortex has emerged (with the same sign as the background shear), and that it has emerged on a much faster time scale than the viscous time scale on which the initial rotation occurred in the unstratified case.

Since the baroclinic source of vorticity is asymmetric, the vortex sheets comprising the baroclinically generated wake are also asymmetric. As time progresses, these sheets roll up into weak but coherent concentrations of vorticity where they are the most strained (see near $(y, z) = (2.5, 6)$ at $t = 10$). Because of the asymmetry in the

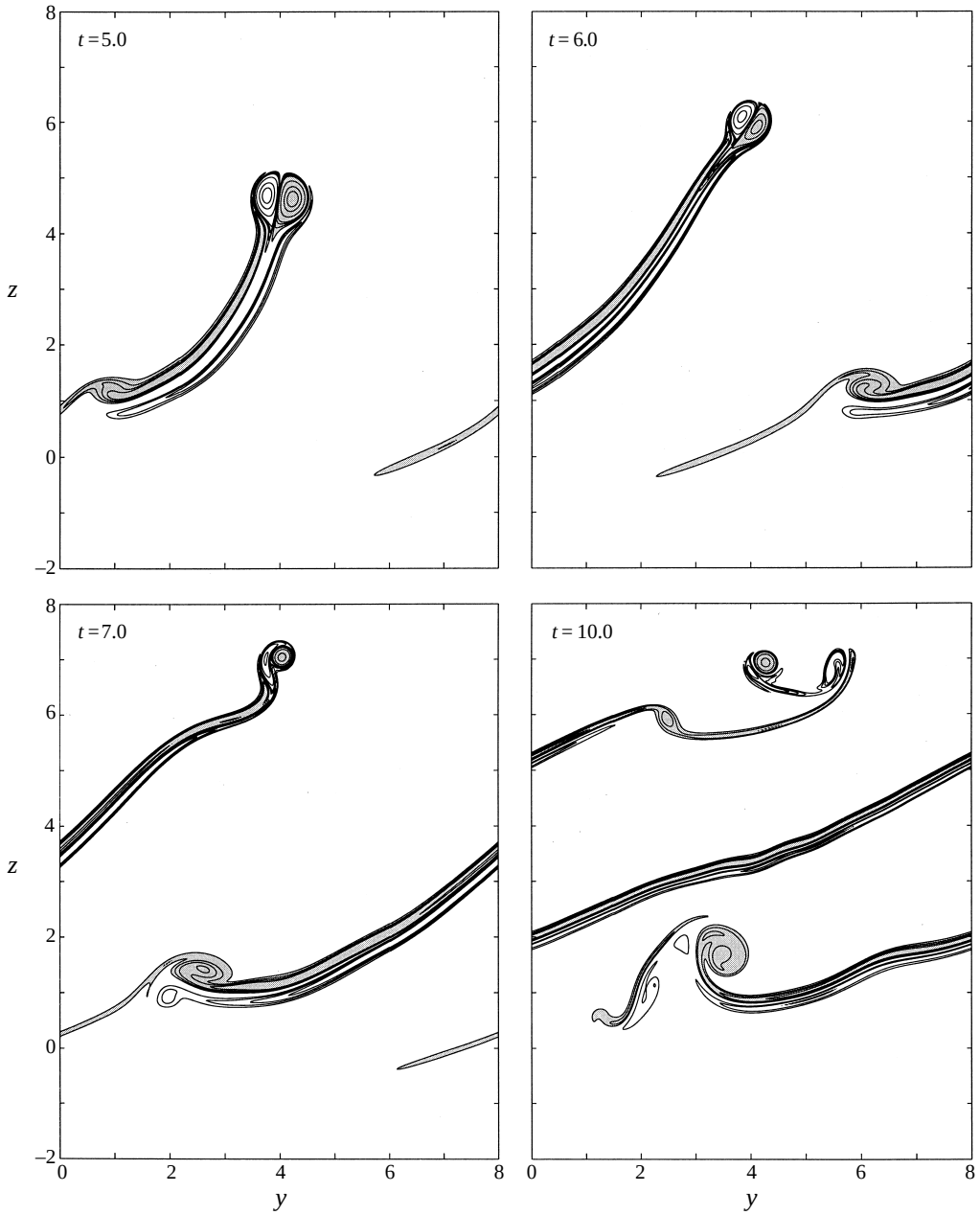

FIGURE 18. As in figure 17 (*a*, *b*), but for more advanced times in the flow of the upwards-propagating vortex pair having $Fr = 2$, $Ri = 1$, and $Re = 1000$.

vortex sheet strength, the long-term flow is dominated by vortices with the same sign as the background shear flow.

The asymmetry in the strength of the vortex sheets also causes the concentrated region of negative vorticity at the lower end of the vortex sheets to be stronger than the concentrated region of positive vorticity (e.g. $t = 7.0$). These regions of vorticity consequently rotate around in the same sense as the rotation of the background shear,

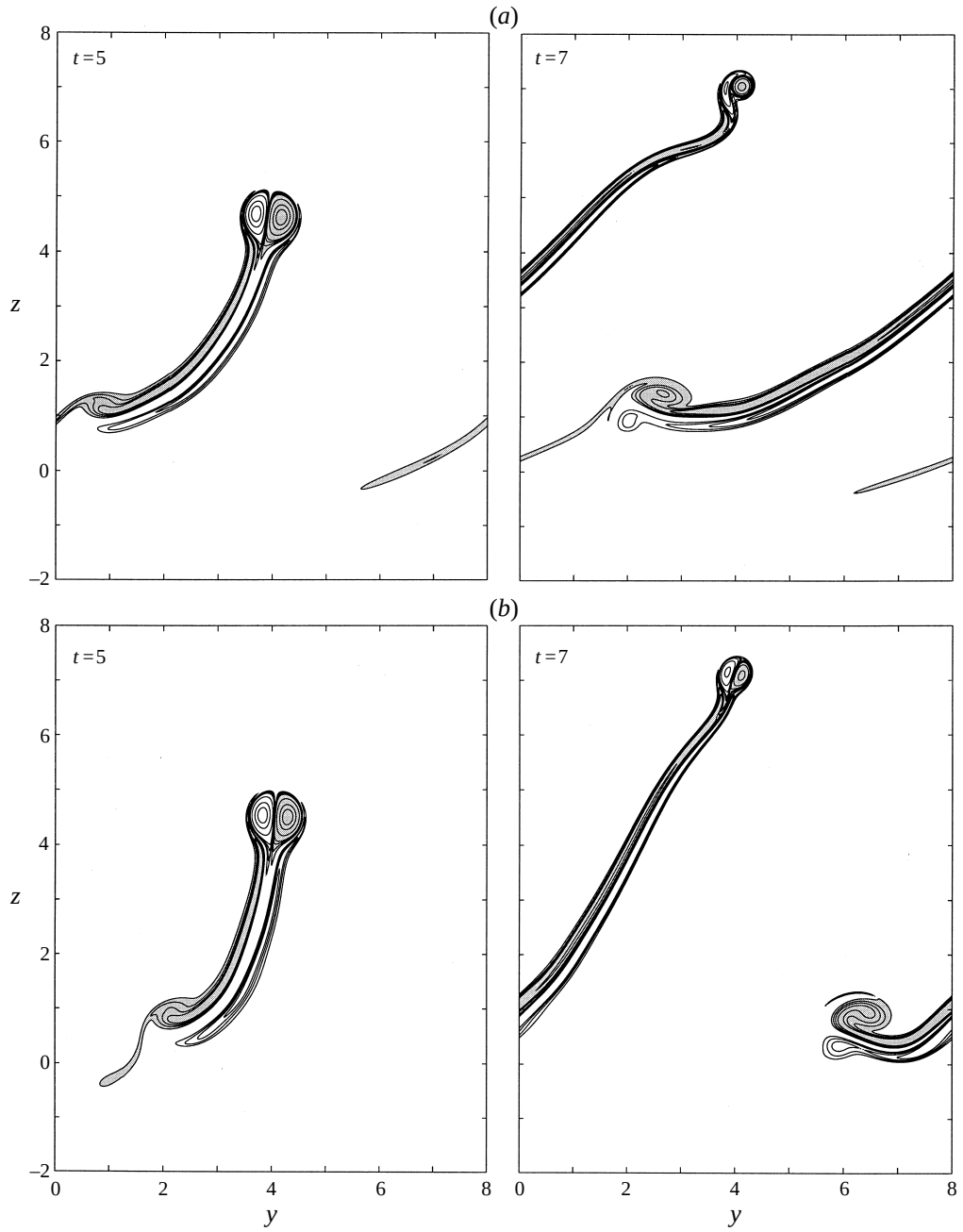

FIGURE 19(*a*, *b*). For caption see facing page.

and this motion apparently prevents vorticity from penetrating below the initial vortex pair position (in contrast to the unsheared case – see figure 3).

5.4. *Consequences of changing Fr, Ri or Re*

We now summarize the possible consequences of changing the values of *Fr*, *Ri* and *Re* on the evolution of vortex pairs in a stratified and sheared fluid. Contours of

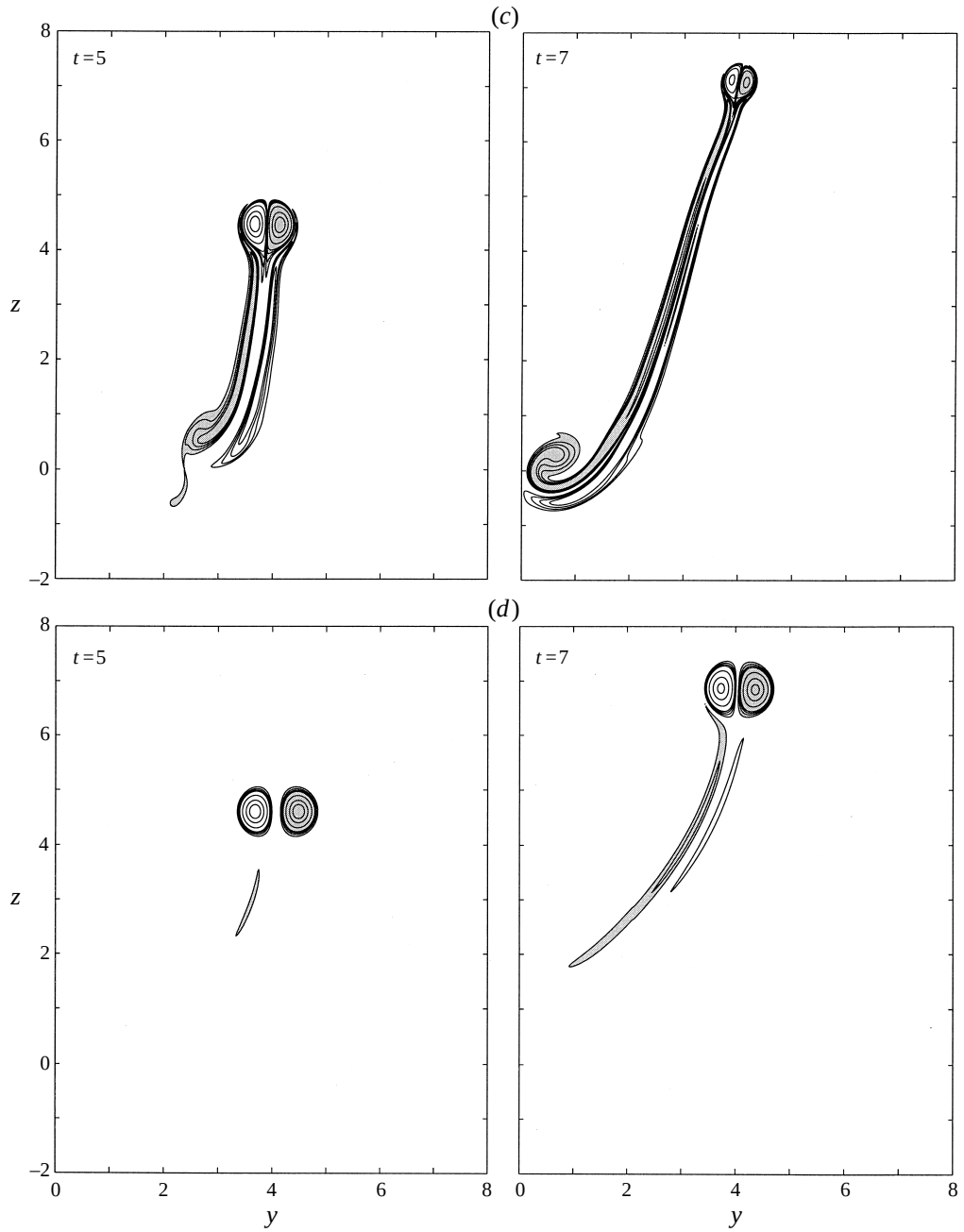

FIGURE 19. As in figure 17 (*a*, *b*), but for the flow of vortex pairs with four different sets of parameters: (*a*) $Fr = 2$ and $Ri = 1$, (*b*) $Fr = 2$ and $Ri = 4$, (*c*) $Fr = 2$ and $Ri = 16$, and (*d*) $Fr = 4$ and $Ri = 1$, all with $Re = 1000$.

vorticity for $Re = 1000$ but for different Fr and Ri are displayed in figure 19 for a part of the evolution.

Consider first the implications of changing the strength of the mean shear while leaving all other parameters fixed. If the shear is weakened (Ri is increased), then

the asymmetry in the flow due to the shear (see figure 15 *b*) is less pronounced, the asymmetry in the baroclinic generation of vorticity (see figure 17 *c*) is less severe, and the asymmetry in the vorticity field itself is not as large (compare the different cases shown in figure 19 at $t = 5$). The initial vortex tilting in the rotational sense opposite that of the mean shear is thus decreased, possibly to zero. With less initial tilting of the vortex pair, the vortex head instability is not given as large an initial amplitude. Although the instability process is still initiated by the preferential detrainment of circulation from the (left-hand) opposite-sign vortex (compare the three cases in figure 19 at $t = 5$), the smaller initial amplitude and delayed onset result in the instability not reaching the saturation amplitude until later in time. This can lead to two possible results. First, it may simply take longer for the primary vortices to detach themselves from the wake vorticity (which occurs when the instability reaches the saturation amplitude), and they will not have retained as much of their circulation, as occurs in the case $Fr = 2$ and $Ri = 4$ (not shown in figure 19). Alternatively, the instability process may be delayed so long that the vortices are too severely depleted and never detach from the wake, as in the case $Fr = 2$ and $Ri = 16$ (as well as $Fr = 4$ and $Ri = 1$). It therefore becomes less likely for a solitary vortex to rapidly emerge as Ri is increased for a fixed value of Fr. The extreme case $Ri \to \infty$ corresponds to the unsheared cases for which we observed the vortex head instability. There, the original vortices were severely depleted and never detached from the wake vorticity, and equal amounts of both signs of vorticity were present at late times in the evolution.

On the other hand, if the shear is made stronger (Ri is decreased) at a fixed value of Fr, then the asymmetries in the flow become more pronounced, and the vortex head instability is initiated with a larger initial amplitude. The more rapid attainment of the saturation amplitude results in the vortices detaching from the wake vorticity before losing as much of their circulation, and the subsequent dynamics lead to the more rapid emergence of a solitary vortex. We conclude that there are not two distinct regimes of behaviour delineated by a critical value of Ri, but rather a continuum depending on the time taken for a solitary vortex to emerge. Of course, this amount of time approaches infinity for some sets of parameters, meaning that a solitary vortex never emerges.

This behaviour will also depend on the value of Fr. As Fr is increased, stratification becomes less important, and, although the shear will still cause an asymmetry in the baroclinic source of vorticity, the baroclinically generated vorticity is no longer as strong as at larger values of Fr (compare the first and fourth cases shown in figure 19). Therefore, a much stronger shear (smaller value of Ri) is needed to produce the same degree of tilting of the vortices and the same strong initial amplitude of the vortex head instability. Conversely, as Fr is decreased, the baroclinic source of vorticity becomes stronger, and small asymmetries in the flow due to the shear will have larger effects. Therefore, a weaker shear (larger value of Ri) can have the same effect when Fr is decreased.

Earlier comparisons (§ 3.2.2) between simulations performed for different Re indicate how these stratified and sheared flows will change if the value of Re is increased. In the sheared cases where tilting of the vortex pair against the shear occurs, we find that the tilting continues until the (left-hand) opposite-sign vortex is sufficiently weak compared to the (right-hand) same-sign vortex that the vortex pair tilts back in the other direction. At larger Re (and/or smaller $\sigma(0)/b_0$), the vortices diffuse outwards more slowly. Therefore, the tilting of the vortex pair should continue longer, as it takes longer for the (left-hand) opposite-sign vortex to lose a significant part of its

circulation. Another way to state this is that as Re is increased at a fixed value of Fr, a weaker shear (larger Ri) will tilt the vortex pair and initialize the instability process as quickly as a stronger shear (smaller Ri) at a lower Re.

6. Summary

In this paper we present and analyse numerical simulations of vertically propagating vortex pairs in stratified and sheared fluids. We discuss the complicated nature of the resolution requirements for the simulations and the difficulty in determining an objective measure for the quality of resolution. To span a range of dynamical responses, we consider the effects of stratification with and without a uniform shear, and with Froude numbers from $1/8$ to ∞ and Richardson numbers from 0 to ∞. Additionally, two different Reynolds numbers are considered.

At all Froude numbers, density stratification leads to baroclinic sources of counter-sign vorticity between and outward from the rising vortex pair. The effects of this baroclinic vorticity, however, are highly dependent on the Froude number and the mean shear.

In the unsheared simulations, for the cases $Fr \geqslant 1$, the relatively strong advection of the primary vortex pair couples with the baroclinic generation of wake vorticity, leading to the formation of trailing vortex sheets. During an initial adjustment phase of two advective time units (independent of Fr), the criteria of Saffman's theory are met, and the trajectories of the vortex pairs follow Saffman's predictions. After this adjustment phase, the advective effect of the accumulated counter-sign vorticity around and trailing each of the primary vortices serves to drive the primary vortices together. The vortices accelerate, and their trajectories are then consistent with the predictions of Crow's theory. At later times, viscous diffusion intervenes, made stronger by the lower values of Re that are numerically tractable. We present a prediction for how far a two-dimensional vortex pair propagates before viscous processes become dominant, and verify that it is confirmed by the simulation results.

For cases with smaller Froude numbers ($Fr \leqslant 1/2$), baroclinic generation of vorticity along with the relatively weak advection of the initial vortex pair leads to more localized regions of secondary vorticity. The separation distance of the vortex pair remains constant during an early adjustment phase whose duration depends on Fr. During this adjustment phase, the trajectories of the vortex pairs follow Saffman's predictions. In fact, the vertical position of the vortex pair remains consistent with the prediction even when the separation distance increases by as much as 50%. The concentrated regions of baroclinically produced vorticity result in the vortices propagating away from one another, and not dominating the flow. At even lower values of the Froude number ($Fr \leqslant 1/8$), the flows are described increasingly well by the linearized equations of motion, so that the evolution is approximately linear gravity wave radiation from a localized source.

When asymmetry is seeded within the initial flow field, instabilities occur. The jet of fluid comprising the baroclinically generated wake of the vortex pair is susceptible to the sinuous mode of a jet instability. Theoretical predictions for the growth rates and spatial scales of the instability modes of the Bickley jet were found to be within 15% of those observed in the simulation for $Re = 1000$, and even closer for higher Re. The sinuous mode in particular grows rapidly enough to reach a critical amplitude and severely complicate the flow evolution.

The primary vortices themselves are susceptible to the vortex head instability, which occurs after viscous diffusion makes possible the alternating detrainment of vorticity

from each vortex. This instability prevents the vortex pair from propagating much further once this stage in the evolution has been reached, and it also complicates the flow. Concentrated vorticity remains near the maximum height attained by the vortex pair very late into the flow evolution, in contrast to the cases in which this instability was not observed.

In the unstratified but sheared case, the evolution of the vortex pair is in good agreement with theory. The vortex pair is advected horizontally by the shear, independent of its upwards propagation, until viscous diffusion leads to the preferential loss of vorticity from the opposite-sign vortex. Consequently, the relatively stronger same-sign vortex rotates the weaker opposite-sign vortex about itself with the same rotational sense as the mean shear flow.

For sheared flows with stratification, the baroclinic source of vorticity is asymmetric due to more rapid flow around the vortices on the (left-hand) upstream side of the vortex pair. In the case $Fr = 2$ and $Ri = 1$, the advective effect of the asymmetrically stronger counter-signed vorticity forming on the (left-hand) upstream side slightly retards the motion of the (left-hand) opposite-sign vortex. However, the tilting of the vortex pair with the rotational sense opposite to the mean shear results in a preferential loss of circulation from the (left-hand) opposite-sign vortex. This in turn causes the vortex pair to tilt back with the same rotational sense as the mean shear flow. This process is the same as that for the vortex head instability, and it leads to the emergence of a solitary vortex (with the same sign as the mean shear vorticity), on a much faster time scale than viscous processes lead to the initial rotation of the vortex pair in the unstratified case. A decrease in Ri at a fixed Fr or an increase in Fr at a fixed Ri reduced the initial amplitude of the vortex head instability, resulting in a solitary vortex emerging much more slowly, if at all. It is important to note that when a solitary vortex is observed to emerge it does not completely dominate the flow evolution (see e.g. Robins & Delisi 1990), and so there is some uncertainty in saying that a solitary vortex has emerged at all (especially in the light of the reformation of one of the vortices in figure 16).

We have greatly benefited from discussions with Mr Robins of NorthWest Research Associates and Dr Øyvind Andreassen of the Norwegian Defense Research Establishment. We would also like to thank the anonymous referees for their substantive comments, and acknowledge the contributions of Dr Keith Julien of the University of Colorado in helping to implement the third-order Runga–Kutta timestepping. This research was supported by the Air Force Office of Scientific Research under grants F49620-95-1-0286 and F49620-96-1-0300, by the National Science Foundation under grant ATM-94-19151, and by the Norwegian Defense Research Establishment. Computational resources were provided in part by the Pittsburgh Supercomputing Center under grant ATM960003P.

REFERENCES

Abramowitz, M. & Stegun, I. A. 1964 *Handbook of Mathematical Functions*. Dover.

Andreassen, Ø., Wasberg, C. E., Fritts, D. C. & Isler, J. R. 1994 Gravity wave breaking in two and three dimensions, I. Model description and comparison of two-dimensional evolutions. *J. Geophys. Res.* **99**, 8095.

Batchelor, G. K. 1959 Small-scale variation of convected quantities like temperature in turbulent fluid. Part 1. General discussion and the case of small conductivity. *J. Fluid Mech.* **5**, 113.

Burnham, D. C. 1972 Effect of ground wind shear on aircraft trailing vortices. *AIAA J.* **10**, 1114.

Canuto, C., Hussaini, M. Y., Quarteroni, A. & Zang, T. A. 1988 *Spectral Methods in Fluid Dynamics*. Springer.

Crow, S. C. 1970 Stability theory for a pair of trailing vortices *AIAA J*. **8**, 2172.

Crow, S. C. 1974 Motion of a vortex pair in a stably-stratified fluid *Poseidon Research Rep*. No. 1.

Crow, S. C. & Bate, E. R. 1976 Lifespan of trailing vortices in a turbulent atmosphere. *J. Aircraft* **13**, 476.

Delisi, D. P., Robins, R. E. & Lucas, R. D. 1991 Initial laboratory observations of the evolution of a vortex pair in a stratified shear flow. *Phys. Fluids* A **3**, 2489.

Drazin, P. G. & Howard, L. N. 1966 Hydrodynamic stability of parallel flow of inviscid fluid. In *Advances in Applied Mechanics*, pp. 1–89. Academic.

Fincham, A. M & Spedding, G. R. 1997 Low cost, high resolution DPIV for measurement of turbulent fluid flow. *Exps. Fluids* **23**, 449.

Garten, J. F. 1997 An investigation of the effects of environmental stratification and shear on the evolution of vertically-propagating vortex pairs. PhD Thesis, University of Colorado.

Greene, G. C. 1986 An approximate model of vortex decay in the atmosphere. *J. Aircraft* **23**, 566.

Harvey, J. K. & Perry, F. J. 1971 Flowfield produced by trailing vortices in the vicinity of the ground. *AIAA J*. **9**, 1659.

Hecht, A. M., Bilanin, A. J. & Hirsh, J. E. 1981 Turbulent trailing vortices in stratified fluids. *AIAA J*. **19**, 691.

Henshaw, W. D., Kreiss, H. O. & Reyna, L. G. 1989 On the smallest scale for the incompressible Navier-Stokes equations. *Theor. Comput. Fluid Dyn.* **1**, 65.

Hill, F. M. 1975 A numerical study of the descent of a vortex pair in a stably stratified atmosphere. *J. Fluid Mech.* **71**, 1.

Jaderberg, L. K. 1980 A method for computing the internal wave field around a nonlinear stratified flow. PhD Thesis, UCLA.

Kolmogorov, A. N. 1941 The local structure of turbulence in incompressible viscous fluid for very large Reynolds numbers. *C. R. Acad. Sci. USSR* **30**, 301.

Lamb, H. 1945 *Hydrodynamics*. Dover.

Lissaman, P. B. S., Crow, S. C., MacCready, P. B., Tombach, I. H. & Bate, E. R. 1973 Aircraft vortex wake descent and decay under real atmospheric effects. *Transportation Systems Center Rep*. FAA-RD-73-120.

Longcope, D. W., Fisher, G. H. & Arendt, S. 1996 The evolution and fragmentation of rising magnetic flux tubes. *Astrophys. J*. **464**, 999.

Moore, D. W. & Saffman, P. G. 1975 The instability of a straight vortex filament in a strain field. *Proc. R. Soc. Lond.* A **346**, 413.

Olsen, J. H., Goldburg, A. & Rogers, M. 1971 Aircraft wake turbulence and its detection. *Proc. Symp. on Aircraft Wake Turbulence, Seattle*.

Pierrehumbert, R. T. 1980 A family of steady, translating vortex pairs with distributed vorticity. *J. Fluid Mech.* **99**, 129.

Rast, M. P. 1997 Solar granulation: a surface phenomenon In *Geophysical and Astrophysical Convection*. Gordon and Breach.

Robins, R. E. & Delisi, D. P. 1990 Numerical study of vertical shear and stratification effects on the evolution of a vortex pair. *AIAA J*. **28**, 661.

Rogers, M. M. & Moin, P. 1987 The structure of the vorticity field in homogeneous turbulent flows. *J. Fluid Mech.* **176**, 33.

Saffman, P. G. 1972 The motion of a vortex pair in a stratified atmosphere *SIAM J. Appl. Maths* **51**, 107.

Saffman, P.G. 1992 *Vortex Dynamics*. Cambridge University Press.

Sarpkaya, T. 1983 Trailing vortices in homogeneous and density-stratified media. *J. Fluid Mech.* **136**, 85.

Schilling, V., Siano, S. & Etling, D. 1996 Dispersion of aircraft emissions due to wake vortices in stratified shear flows: A two-dimensional numerical study. *J. Geophys. Res.* **101**, 20965.

Scorer, R. S. & Davenport, L. J. 1970 Contrails and aircraft downwash. *J. Fluid Mech.* **43**, 451.

Spalart, P. R. 1996 On the motion of laminar wing wakes in a stratified fluid. *J. Fluid Mech.* **327**, 139.

Spalart, P. R., Moser, R. D. & Rogers, M. M. 1991 Spectral methods for the Navier-Stokes equations with one infinite and two periodic directions *J. Comput. Phys.* **96**, 297.

Tomassian, J. D. 1979 The motion of a vortex pair in a stratified medium. PhD Thesis, UCLA.

Tsai, C.-Y. & Widnall, S. E. 1976 The stability of short waves on a straight vortex filament in a weak externally imposed strain field. *J. Fluid Mech.* **73**, 721.

Turner, J. S. 1960 A comparison between buoyant vortex rings and vortex pairs. *J. Fluid Mech.* **7**, 419.

Werne, J. 1993 Structure of hard-turbulent convection in two dimensions: Numerical evidence. *Phys. Rev.* E **48**, 1020